

New luminescent tetracoordinate boron complexes: an in-depth experimental and theoretical characterisation and their application in OLEDs

Paramasivam Krishnamoorthy,^{a,h} Carina B. Fialho,^a Tiago F. C. Cruz,^a Ana I. Rodrigues,^a Bruno Ferreira,^a Clara S. B. Gomes,^{a,e,i} Diogo Vila-Viçosa,^c Ana Charas,^d José M. S. S. Esperança,^e Luís F. Vieira Ferreira,^f Maria José Calhorda,^c António L. Maçanita,^{a,b}
Jorge Morgado^{d,g} and Pedro T. Gomes^{*,a,b}

^a Centro de Química Estrutural, Instituto Superior Técnico, Universidade de Lisboa, Av. Rovisco Pais, 1049-001 Lisboa, Portugal.

^b Departamento de Engenharia Química, Instituto Superior Técnico, Universidade de Lisboa, Av. Rovisco Pais, 1049-001 Lisboa, Portugal.

^c BioISI - Biosystems & Integrative Sciences Institute, Departamento de Química e Bioquímica, Faculdade de Ciências, Universidade de Lisboa, Campo Grande, Ed. C8, 1749-016 Lisboa, Portugal.

^d Instituto de Telecomunicações, Av. Rovisco Pais, 1049-001 Lisboa, Portugal.

^e LAQV-REQUIMTE, Departamento de Química, Faculdade de Ciências e Tecnologia, Universidade NOVA de Lisboa, 2829-516 Caparica, Portugal

^f BSIRG – Biospectroscopy and Interfaces Research Group, IBB-Institute for Bioengineering and Biosciences, Instituto Superior Técnico, Universidade de Lisboa, 1049-001 Lisboa, Portugal

^g Department of Bioengineering, Instituto Superior Técnico, Universidade de Lisboa, Av. Rovisco Pais, 1049-001 Lisboa, Portugal.

^h Centre for Environmental Research, Department of Chemistry, Kongu Engineering College, Perundurai, Erode 638 060, India

ⁱ UCIBIO-REQUIMTE, Departamento de Química, Faculdade de Ciências e Tecnologia, Universidade NOVA de Lisboa, 2829-516 Caparica, Portugal.

* Corresponding author: Pedro T. Gomes; E-mail: pedro.t.gomes@tecnico.ulisboa.pt

Index

Crystallographic and molecular structure data of boron complexes 3 , 4 , 6 and 7	S3
Thermogravimetric Analysis (TGA)	S8
Computational studies – Energy Decomposition Analysis and binding energy	S10
NMR spectra of complexes 3-7	S13
Variable-temperature (VT) NMR spectra of complex 4	S23
Van't Hoff plot for the equilibrium between tetracoordinate and tricoordinate isomers of complex 4	S27
Computational studies – Energy profile for the conversion of complex 4 into the tricoordinate isomers 4_{3E-endo} and 4_{3E-exo} and comparison with mononuclear boron complexes 3 , 5 , 6 and 8	S28
Computational studies – Ground state and first excited state optimised structure geometries of boron complexes 3-9	S32
Computational studies – Frontier orbitals and composition of the lower energy electronic transitions in boron complexes 4 and 6	S35
Computational studies – Calculated HOMOs and LUMOs energies for complexes 3-9 using different methods.....	S36
Computational studies – Calculated absorption energies and first excited state lifetimes for complexes 3-9 using different methods.....	S37
Computational studies – Composition of the lower energy electronic transitions in complexes 4 and 6	S38
Computational studies – Calculated energies of $S_1 \rightarrow S_0$ transition for complexes 3-2 using different methods.....	S39
Electrochemical properties	S40
Electroluminescence performance	S42

Crystallographic and molecular structure data of boron complexes 3, 4, 6 and 7

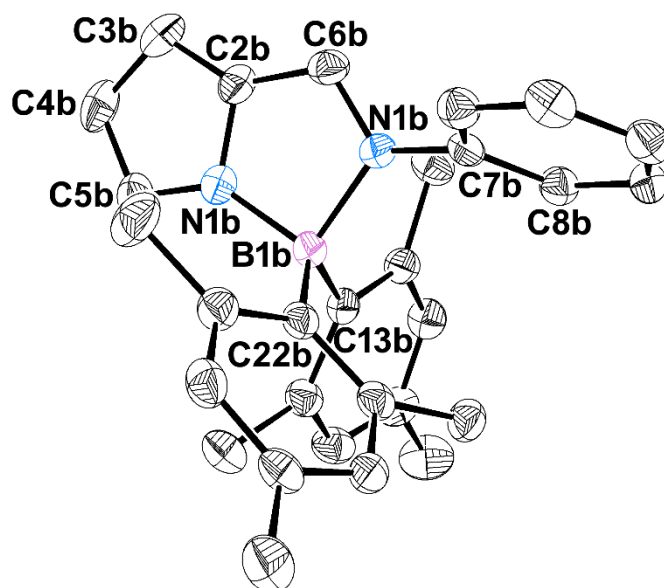


Figure S1. Perspective view of the molecular structure of 2-iminopyrrolyl boron complex 4 (molecule B), using 50% probability level ellipsoids. All calculated hydrogen atoms were omitted for clarity.

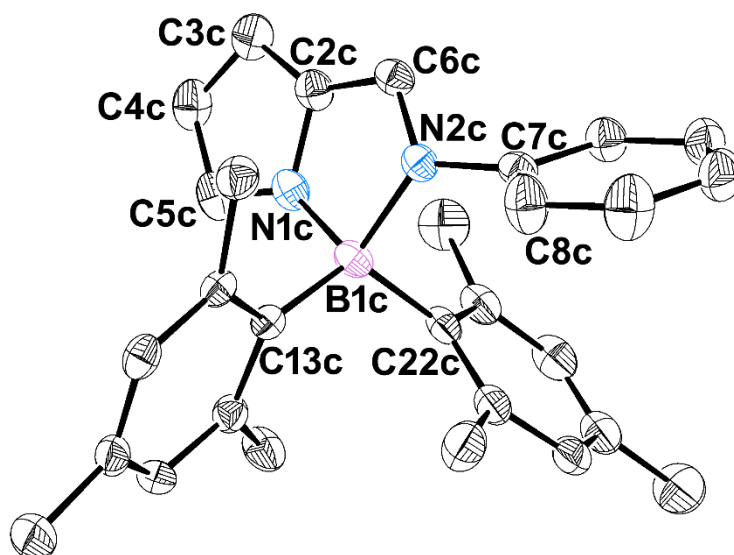


Figure S2. Perspective view of the molecular structure of 2-iminopyrrolyl boron complex 4 (molecule C), using 50% probability level ellipsoids. All calculated hydrogen atoms were omitted for clarity.

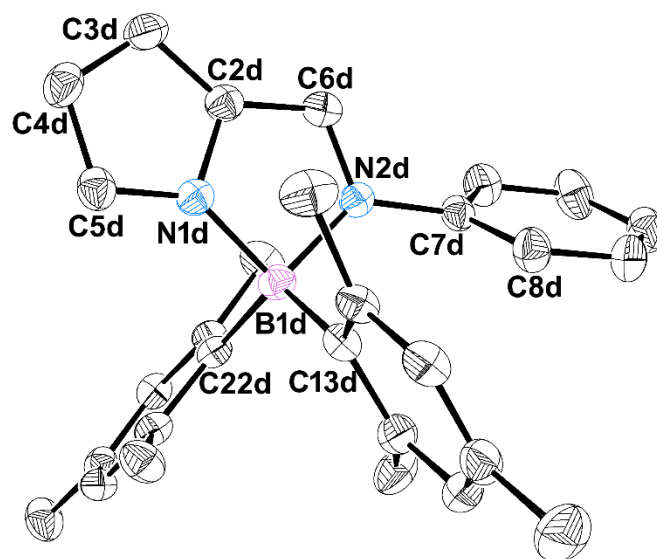


Figure S3. Perspective views of the molecular structure of 2-iminopyrrolyl boron complex **4** (molecule D), using 50% probability level ellipsoids. All calculated hydrogens atoms were omitted for clarity.

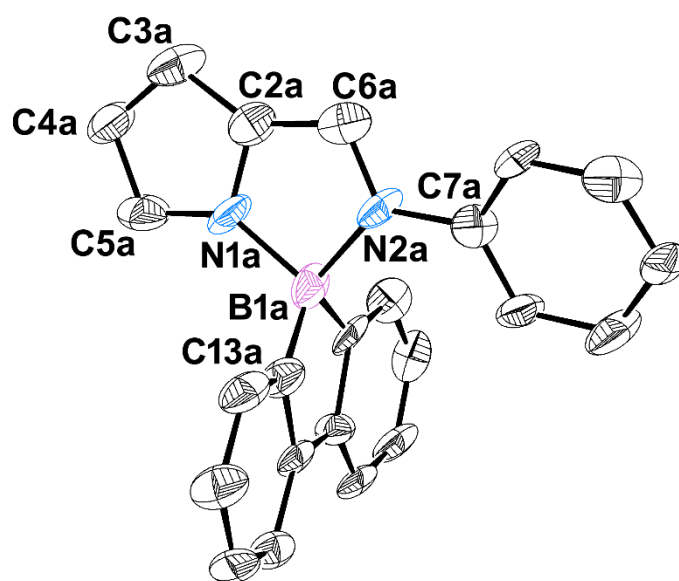


Figure S4. Perspective view of the molecular structure of 2-iminopyrrolyl boron complex **6** (molecule A), using 50% probability level ellipsoids. All calculated hydrogen atoms were omitted for clarity.

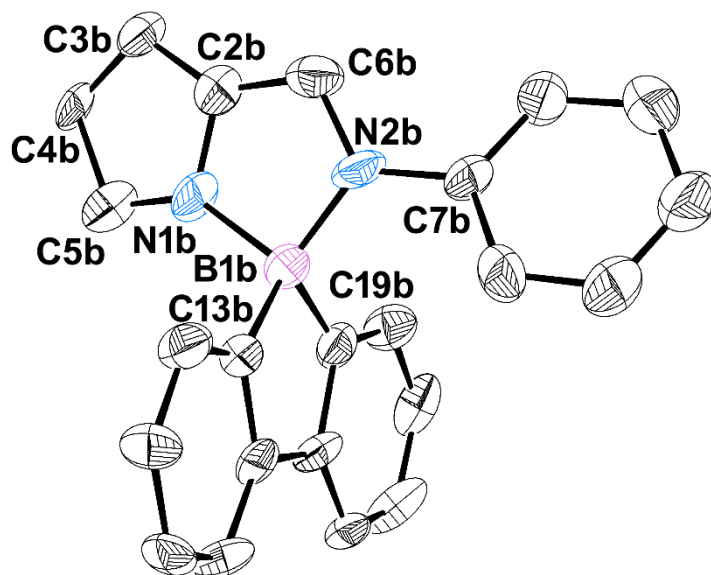


Figure S5. Perspective view of the molecular structure of 2-iminopyrrolyl boron complex **6** (molecule B), using 50% probability level ellipsoids. All calculated hydrogen atoms were omitted for clarity.

Table S1. Selected bond distances (Å) and angles (°) for compounds **3**, **4**, **6** and **7**.

	3	4				6		7
		<i>molecule A</i>	<i>molecule B</i>	<i>molecule C</i>	<i>molecule D</i>	<i>molecule A</i>	<i>molecule B</i>	
<i>Bond distances</i>								
N1–B1	1.537(5)	1.589(3)	1.581(3)	1.573(3)	1.589(2)	1.570(10)	1.592(10)	1.555(2)
N2–B1	1.603(4)	1.682(2)	1.648(3)	1.654(3)	1.664(3)	1.613(11)	1.562(11)	1.602(2)
N1–C2	1.370(4)	1.381(2)	1.383(3)	1.385(2)	1.371(2)	1.357(10)	1.382(10)	1.385(2)
N1–C5	1.353(4)	1.354(2)	1.348(3)	1.350(3)	1.345(2)	1.360(10)	1.342(10)	1.343(2)
C2–C6	1.410(4)	1.396(2)	1.398(3)	1.401(3)	1.412(3)	1.432(11)	1.388(11)	1.392(2)
N2–C6	1.305(4)	1.309(2)	1.313(2)	1.309(2)	1.305(2)	1.284(9)	1.301(8)	1.3218(19)
N2–C7	1.431(4)	1.448(2)	1.437(2)	1.441(2)	1.450(2)	1.452(9)	1.427(10)	1.4186(19)
B1–E1 ^a	1.379(4)	1.626(3)	1.638(3)	1.627(3)	1.621(3)	1.598(11)	1.652(12)	1.631(2)
B1–E2 ^b	1.381(4)	1.643(3)	1.640(3)	1.640(3)	1.639(3)	1.600(12)	1.593(11)	1.630(2)
<i>Bond angles</i>								
N1–B1–N2	97.0(2)	93.41(13)	94.01(14)	94.49(14)	93.49(13)	94.3(6)	96.5(6)	96.62(11)
C5–N1–C2	107.9(3)	106.48(16)	107.17(16)	107.36(17)	107.62(15)	107.0(6)	109.8(7)	107.83(13)
C2–N1–B1	111.0(2)	112.85(14)	112.48(16)	112.40(16)	112.58(15)	113.1(7)	108.9(7)	110.90(12)
C5–N1–B1	140.9(3)	140.34(16)	139.35(18)	139.81(17)	139.39(17)	139.9(7)	141.1(7)	141.27(14)
C6–N2–C7	123.9(3)	115.46(15)	119.01(17)	119.29(16)	117.76(16)	121.0(7)	121.8(7)	124.01(12)
C6–N2–B1	110.6(2)	110.69(14)	111.41(16)	110.71(16)	111.75(14)	121.0(7)	112.5(7)	110.32(12)
C7–N2–B1	125.3(2)	132.82(14)	126.56(15)	126.84(15)	129.57(14)	126.6(6)	125.4(6)	125.20(12)
E1–B1–E2	109.9(3)	113.22(16)	116.34(16)	116.51(16)	116.15(15)	100.7(6)	99.6(6)	117.27(13)
E1–B1–N1	112.9(3)	120.39(16)	104.63(15)	104.43(16)	118.73(15)	116.2(6)	112.1(7)	107.53(13)
E2–B1–N1	114.3(3)	103.79(15)	119.21(15)	119.06(15)	102.81(14)	114.9(7)	113.8(6)	113.37(12)
E1–B1–N2	111.8(3)	104.63(15)	117.85(16)	120.15(14)	104.42(15)	115.9(7)	117.8(6)	112.88(12)
E2–B1–N2	110.3(3)	120.84(15)	103.32(15)	100.98(15)	119.82(16)	115.7(6)	117.8(8)	107.33(12)
$\omega_{(B1)}$ ^c	91.13(12)	-77.47(8)	-79.05(7)	77.27(8)	78.16(7)	90.4(3)	89.2(3)	85.81(6)
$\varphi_{(Pyr-Ph)}$ ^d	26.58(12)	-57.53(7)	66.98(7)	64.19(9)	57.37(9)	21.7(3)	26.0(3)	23.72(10)
C6–N2–C7–Cx ^e	-24.0(5)	59.2(2)	53.8(2)	-52.2(2)	-61.8(2)	19.3(10)	-22.6(11)	-14.9(2)

^a E1 = F1 (**3**), C13 (**4** and **6**) and C10 (**7**); ^b E2 = F2 (**3**), C22 (**4**), C19 (**6**) and C16 (**7**); ^c Dihedral angle between N1–B1–N2 and E1–B1–E2; ^d Dihedral angle between the average planes of the 2-iminopyrrolyl (Pyr) moiety and of the iminic *N*-phenyl ring (Ph); ^e Cx = C8 or C12.

Table S2. Crystal data and structure refinement for compounds **3**, **4**, **6** and **7**.

Compound	3	4	6	7
Formula	C ₁₁ H ₉ F ₂ BN ₂	C ₂₉ H ₃₁ BN ₂	C ₂₃ H ₁₇ BN ₂	C ₄₈ H ₃₂ B ₂ F ₂₀ N ₄ O ₂
<i>M</i>	218.01	418.37	332.19	1098.39
λ (Å)	0.71073	0.71073	0.71073	0.71073
<i>T</i> (K)	150(2)	150(2)	150(2)	150(2)
crystal system	Monoclinic	Triclinic	Monoclinic	Triclinic
space group	<i>P</i> 2 ₁ / <i>n</i>	<i>P</i> -1	<i>P</i> 2 ₁ / <i>c</i>	<i>P</i> -1
<i>a</i> (Å)	6.413(3)	16.9181(13)	17.677(4)	8.9402(4)
<i>b</i> (Å)	7.019(3)	17.0427(13)	11.145(3)	10.6602(5)
<i>c</i> (Å)	22.215(8)	17.8177(12)	17.729(4)	12.8486(6)
α (deg)	90	75.611(3)	90	105.370(2)
β (deg)	95.590(14)	71.293(3)	97.743(12)	97.060(2)
γ (deg)	90	87.992(4)	90	95.9220(10)
<i>V</i> (Å ³)	995.2(6)	4707.7(6)	3461.1(13)	1159.93(9)
<i>Z</i>	4	8	8	1
<i>Z</i> '	1	4	2	0.5
ρ_{calc} (g cm ⁻³)	1.455	1.181	1.275	1.572
μ (mm ⁻¹)	0.113	0.068	0.074	0.152
θ_{max} (deg)	25.66	25.77	25.34	26.19
total data	3960	41526	54163	14831
unique data	1100	11977	1773	3567
<i>R</i> _{int}	0.0509	0.0510	0.3189	0.0451
<i>R</i> [<i>I</i> > 3 σ (<i>I</i>)]	0.0594	0.055	0.1233	0.0367
<i>wR</i> ₂	0.1459	0.1216	0.2685	0.0881
Goodness of fit	0.958	1.073	0.911	1.059
ρ_{min}	-0.259	-0.519	-0.427	-0.219
ρ_{max}	0.232	0.684	0.350	0.249

Thermogravimetric Analysis (TGA)

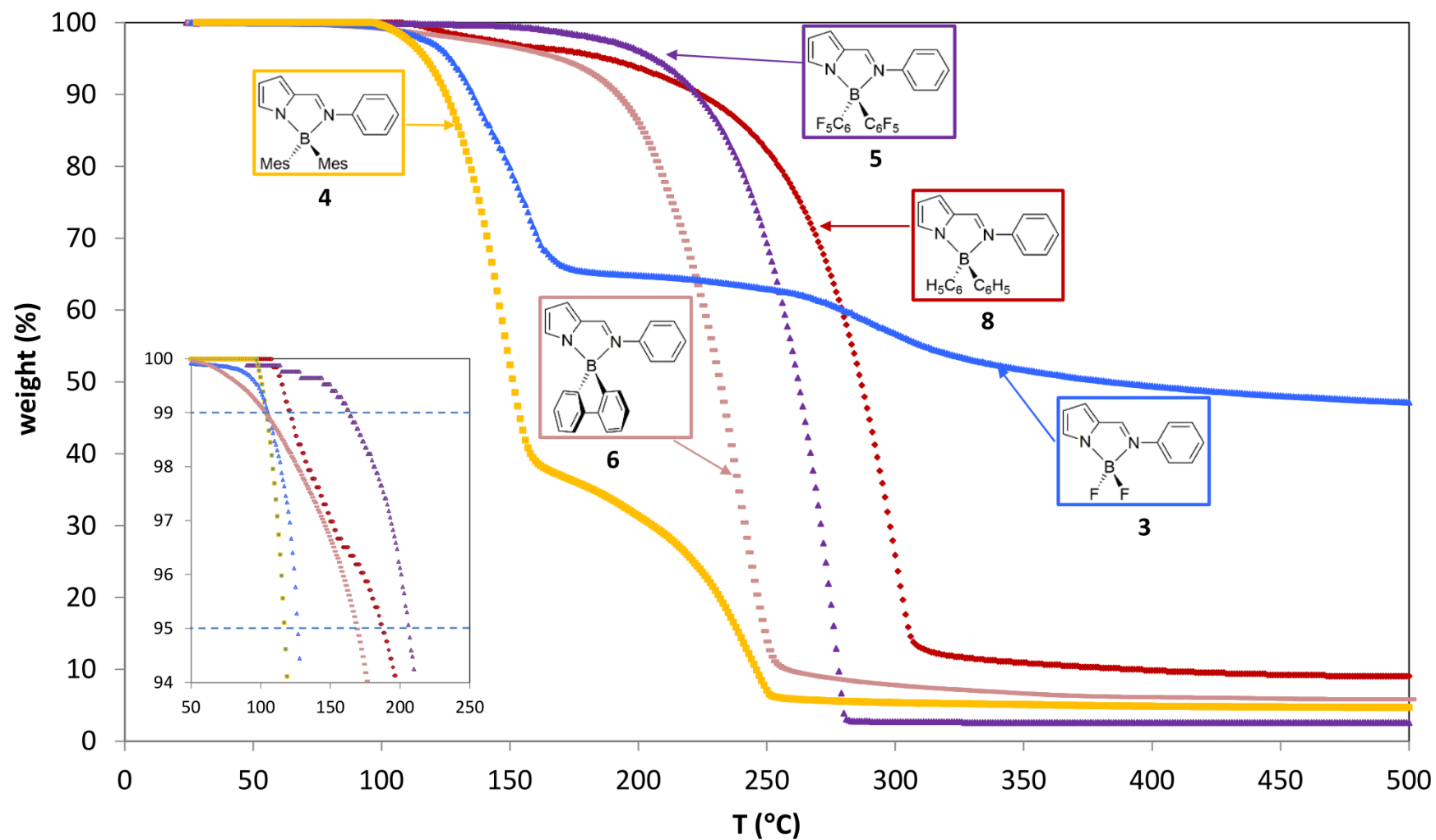


Fig. S6. TGA thermograms of complexes **3**, **4**, **5**, **6** and **8**. The inset of the picture represents the beginning of the decomposition with two dashed lines, one for the 1% weight loss, and another for the 5% weight loss.

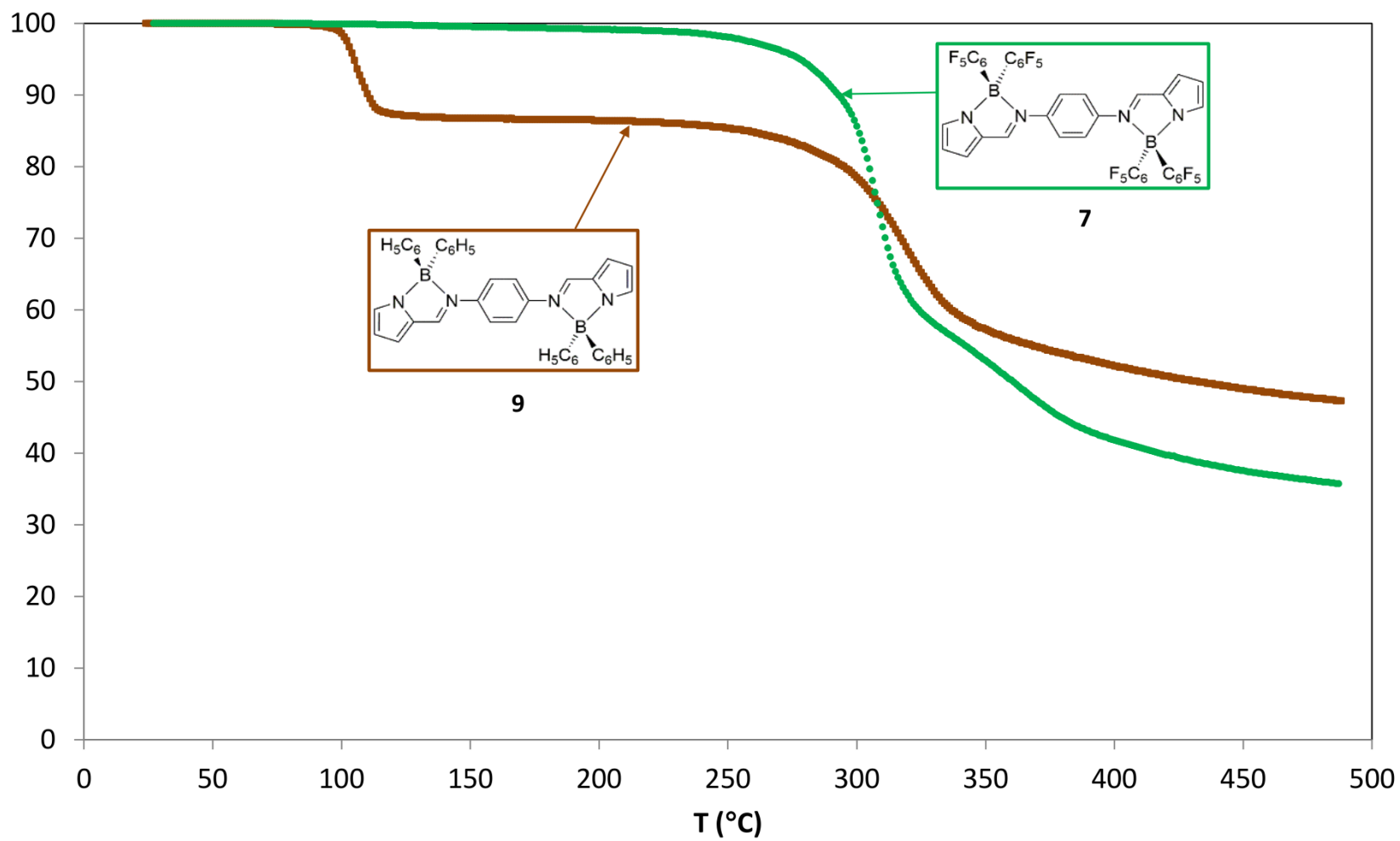


Fig. S7. TGA thermograms of complexes **7** and **9**.

Computational studies – Energy Decomposition Analysis and binding energy

The complexes **3-9** share 2-iminopyrrolyl ligands and therefore the binding energies of this ligand to the boron fragment (BX₂) could be related to their thermal stability described above (Figures S5 and S6 and Table 1). This led us to perform an Energy Decomposition Analysis (EDA) to understand the differences between them. The binding energy (BE) between two fragments in a molecule is the difference between the energy of the molecule and the sum of the energies of the fragments in their optimised geometry. On the other hand, it is possible to define the interaction energy (ΔE_{int}) as the difference between the energy of the molecule and the sum of the energies of the fragments when they keep the same geometry as they have in the molecule. The energy needed to convert this geometry into the geometry with the lowest energy is called the reorganization energy (E_{reorg}). Thus:

$$BE = \Delta E_{int} + \Delta E_{reorg}$$

The Energy Decomposition Analysis (EDA) gives a different way of interpreting the ΔE_{int} terms by decomposing them:

$$\Delta E_{int} = \Delta E_{Pauli} + \Delta E_{elec} + \Delta E_{orb}$$

where ΔE_{Pauli} is a repulsive term representing the destabilizing interactions between occupied orbitals, while the attractive terms ΔE_{elec} and ΔE_{orb} include the electrostatic interaction between the rigid fragments, and the interaction between orbitals, such as HOMO-LUMO interactions and polarization (mixing of empty and occupied levels of each fragment occurring in the presence of another fragment), respectively.

When the calculations include the effect of the solvent, as happens in this study, another term (ΔE_{solv}), arising from the interactions of molecules and fragment with the solvent, also contributes to the interaction energy:

$$\Delta E_{int} = \Delta E_{Pauli} + \Delta E_{elec} + \Delta E_{orb} + \Delta E_{solv}$$

The EDA values are given in Table S5. In the five mononuclear complexes, the binding energy (BE, kcal mol⁻¹) increases from **4** (B(2,4,6-Me₃-C₆H₂)₂, -77.7) < **8** (B(C₆H₅)₂, -112.0) < **5** (B(C₆F₅)₂, -131.5) < **6** (9-borafluorenyl, -143.0) < **3** (BF₂, -153.4) and follows almost the same order of the interaction energy ΔE_{int} . This indicates that the reorganizing energies do not change the trend. Indeed, the 2-iminopyrrolyl ligand requires ~21.5 – 23.8 kcal mol⁻¹ to relax from the geometry it adopts in the complex to the optimised one. It is practically the same value for all the complexes. The relaxation of the BX₂ fragment involves a change in the F-B-F or C-B-C angle observed in the

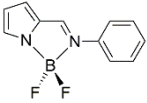
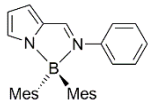
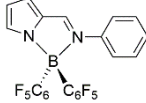
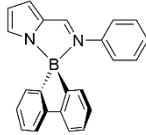
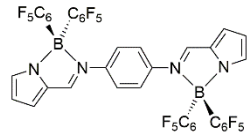
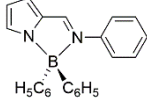
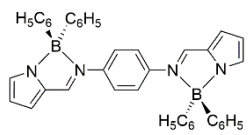
complex to 180° in the free fragment (except in the case of the chelated 9-borafluorenyl fragment in **6**). The maximum reorganization energy (kcal mol⁻¹) occurs for the F-B-F in **3** (67.2), followed by **4** (61.2), **5** (51.4), **8** (45.8) and, not surprisingly, the more rigid **6** (31.9).

The ΔE_{steric} term shows the balance between the Pauli repulsion and the attractive electrostatic term. It is negative for all complexes except **4**. Since ΔE_{orb} and ΔE_{solv} are not very different for the five species, we assign the lowest BE of **4** to the large ΔE_{Pauli} repulsive term associated with a low ΔE_{elec} . Complex **3**, with low ΔE_{Pauli} and very large ΔE_{elec} displays the highest BE. The other fluorinated complex, **5**, also has a large ΔE_{elec} but high ΔE_{Pauli} , the resulting ΔE_{steric} being similar to that of **6**. The smaller solvent penalty and reorganization energy of the BX₂ fragment confer a higher BE to **6** than to **5**. Complex **8** has a less negative ΔE_{steric} term.

The BEs (kcal mol⁻¹) of the pentafluorinated derivatives are larger than those of the hydrogenated analogues. Indeed, the BE of **5** [B(C₆F₅)₂] is -131.5 and of **8** [B(C₆H₅)₂] is -112.0, while for the binuclear **7** and **9** are -270.1 and -233.5, respectively, reflecting the main pattern observed in the experimental thermal analysis (Table S3). This behaviour is assigned mainly to the larger attractive electrostatic and covalent interactions in the fluorinated species. The ΔE_{orb} term is for both **7** and **9** more negative than in the mononuclear species (twice owing to the double number of B-N bonds formed) and is higher for the fluorinated **7**, which has a higher BE and ΔE_{int} , despite the higher solvent destabilization.

Complex **4** [B(2,4,6-Me₃-C₆H₂)₂] with the lowest decomposition energy has the weakest binding energy (-77.7). The high binding energy of complex **3** [BF₂] does not agree with the easy thermal decomposition, but this may be assigned to kinetic factors, which caused decomposition of the compound even in normal handling. The relative thermal stability of **6** (9-borafluorenyl), as measured by T_{dec 5%} (Table 1), is slightly different than might be anticipated from its BE of -143.0.

Table S3. Energy Decomposition Analysis (EDA) of complexes **3-9**.

EDA terms	 3	 4	 5	 6	 7	 8	 9
ΔE_{Pauli}	213.6	336.2	314.8	269.9	628.0	297.3	595.5
ΔE_{elec}	-338.6	-314.2	-339.7	-304.6	-759.9	-311.4	-700.4
ΔE_{steric}	-125.0	22.0	-24.9	-34.7	-131.9	-14.1	-104.9
ΔE_{orb}	-251.1	-269.7	-292.3	-263.2	-582.4	-261.5	-523.5
ΔE_{solv}^a	-132.5	-87.3	-110.5	-99.4	-291.3	-95.2	-256.8
ΔE_{int}	-243.6	-160.4	-206.7	-198.5	-423.0	-180.4	-371.6
$\Delta E_{reorg-ImPyrr}$	23.0	21.5	23.8	23.6	48.3	22.6	46.5
$\Delta E_{reorg-BX_2}$	67.2	61.2	51.4	31.9	104.6	45.8	91.6
ΔE_{reorg}	90.2	82.7	75.2	55.5	152.9	68.4	138.1
BE	-153.4	-77.7	-131.5	-143.0	-270.1	-112.0	-233.5

^a The solvation energy of the fragments is subtracted.^{23c}

NMR spectra of complexes 3-7

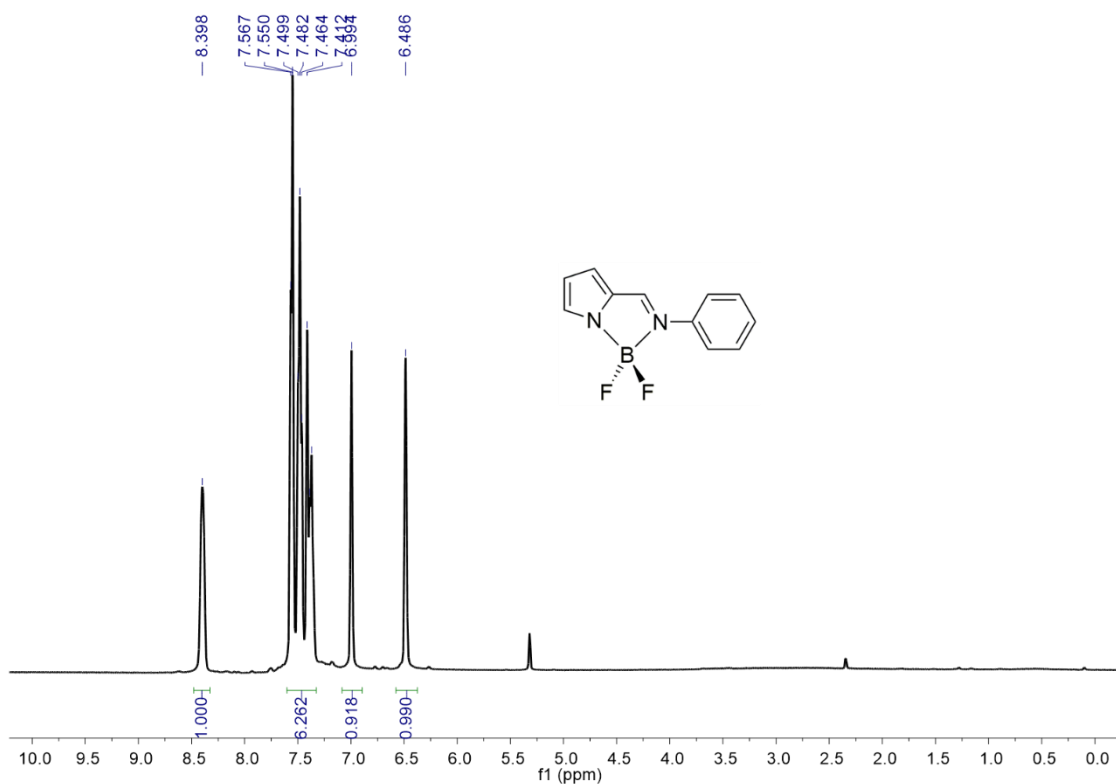


Figure S8. ^1H NMR spectrum (400 MHz, CD_2Cl_2) of complex **3**.

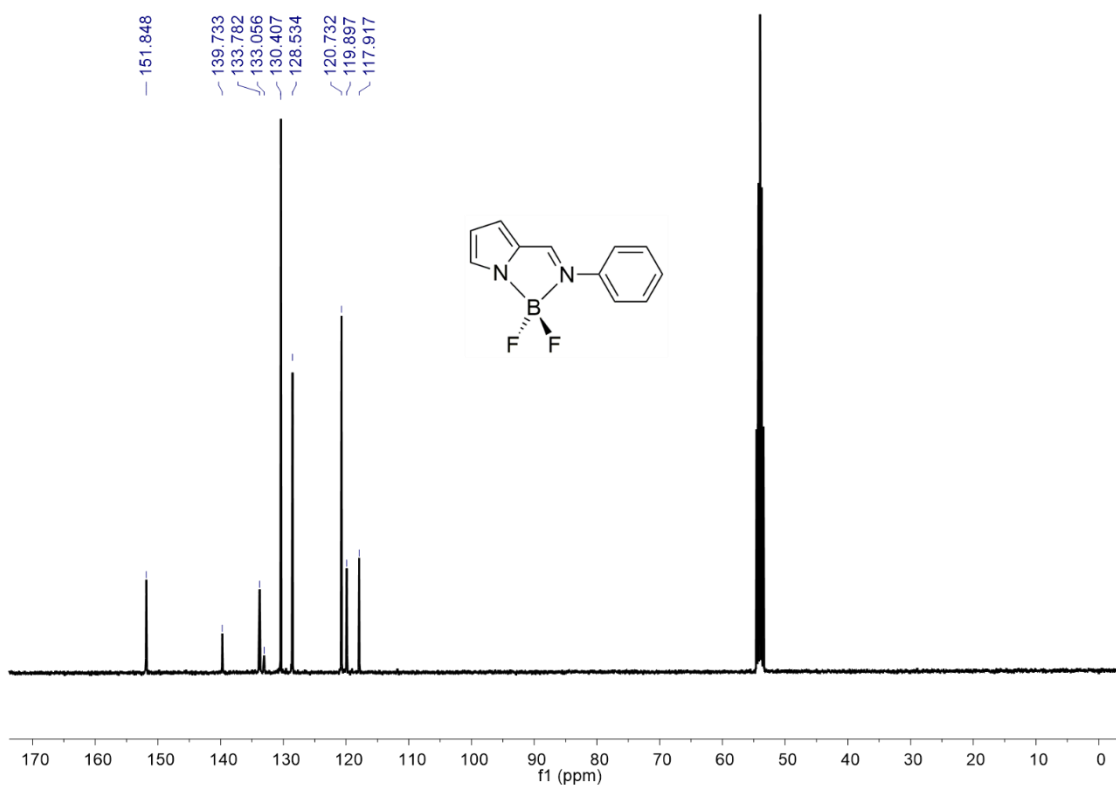


Figure S9. $^{13}\text{C}\{^1\text{H}\}$ NMR spectrum (100.61 MHz, CD_2Cl_2) of complex **3**.

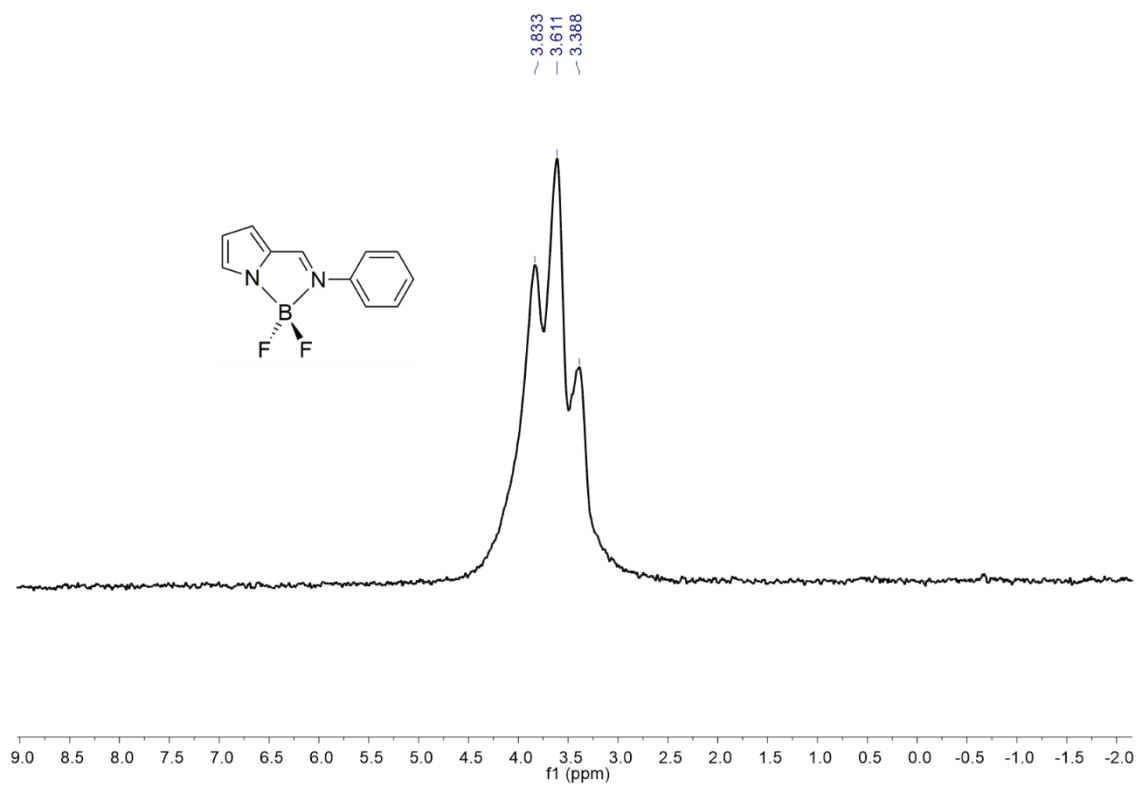


Figure S10. ^{11}B NMR spectrum (128.35 MHz, CD_2Cl_2) of complex **3**.

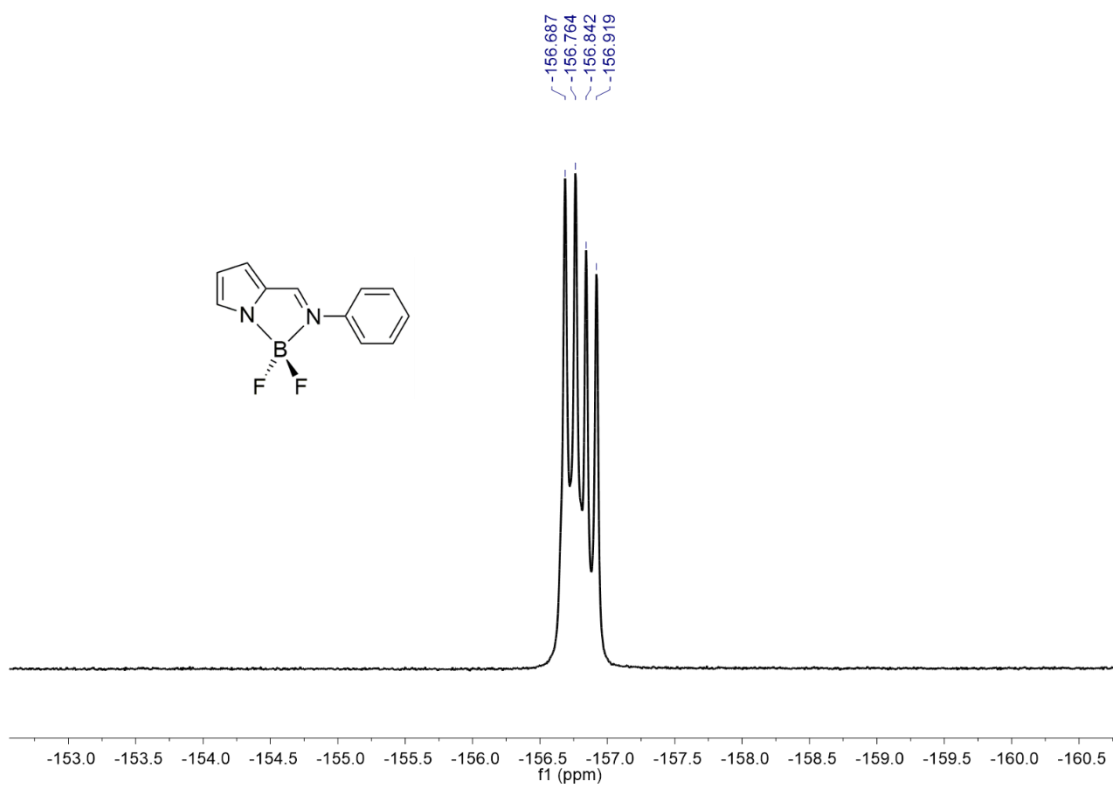


Figure S11. $^{19}\text{F}\{^1\text{H}\}$ NMR spectrum (376.50 MHz, CD_2Cl_2) of complex **3**.

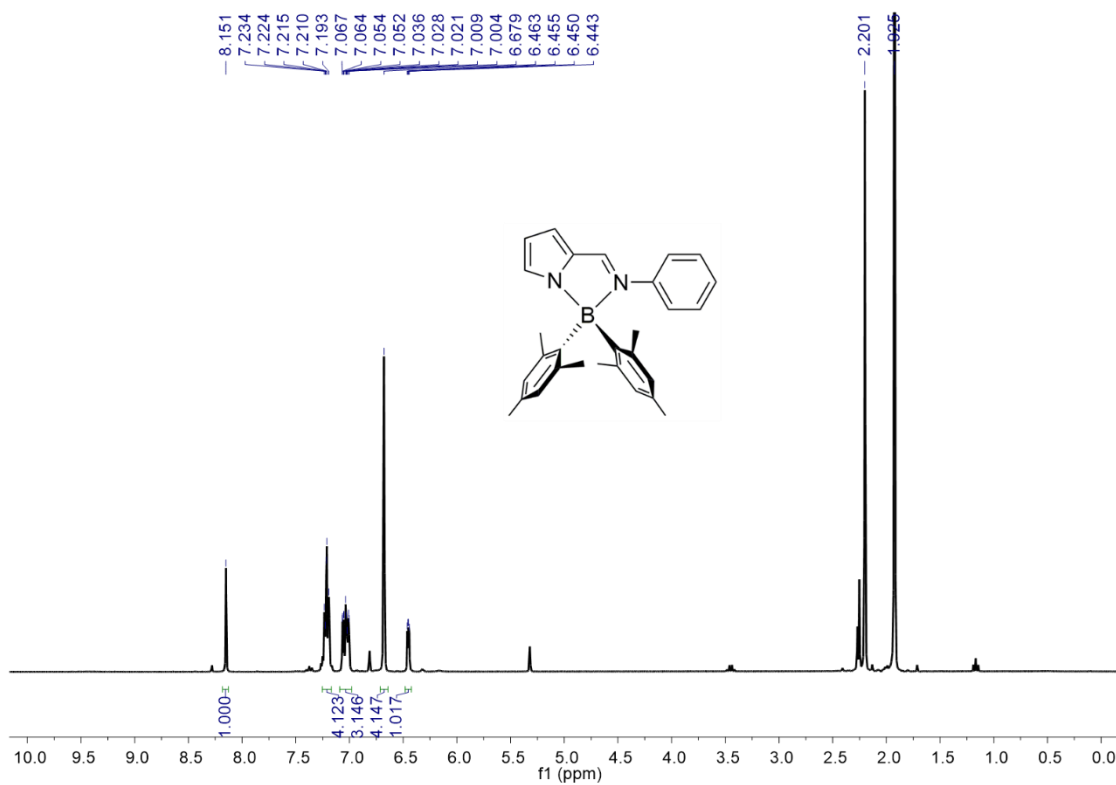


Figure S12. ¹H NMR spectrum (300 MHz, CD₂Cl₂) of complex 4.

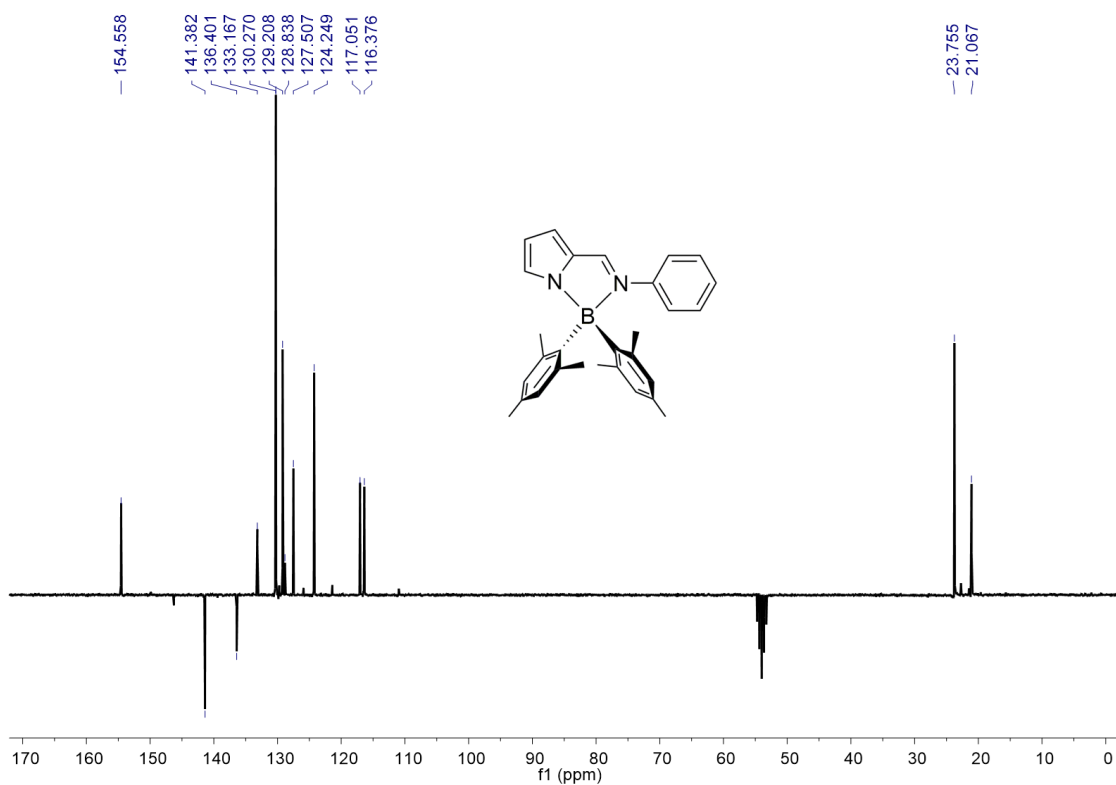


Figure S13. ¹³C APT NMR spectrum (75.47 MHz, CD₂Cl₂) of complex 4.

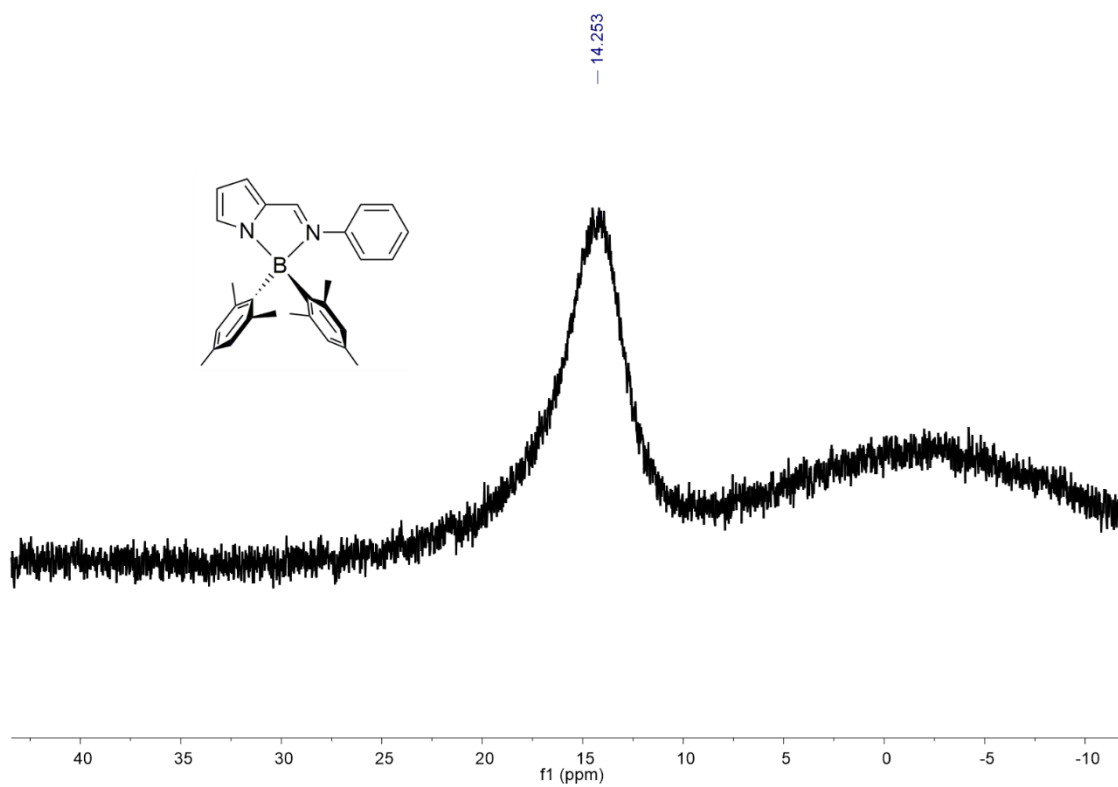


Figure S14. ^{11}B NMR spectrum (96.27 MHz, CD_2Cl_2) of complex **4**.

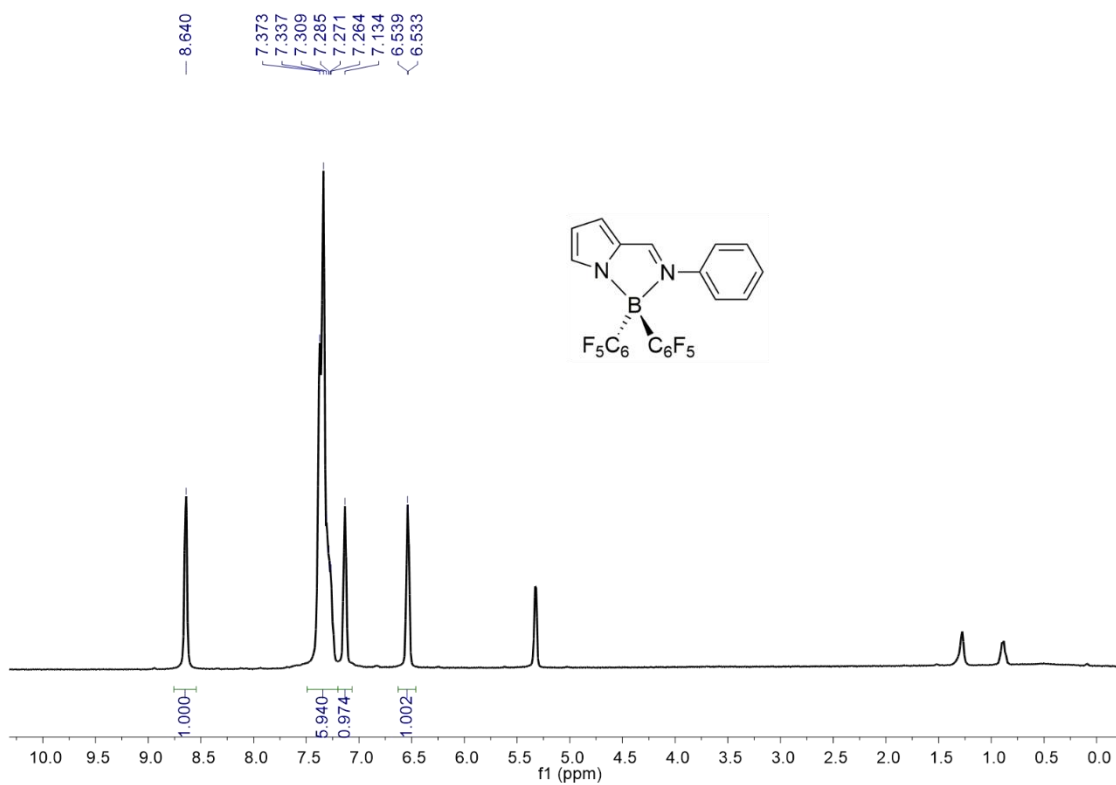


Figure S15. ¹H NMR spectrum (300 MHz, CD₂Cl₂) of complex 5.

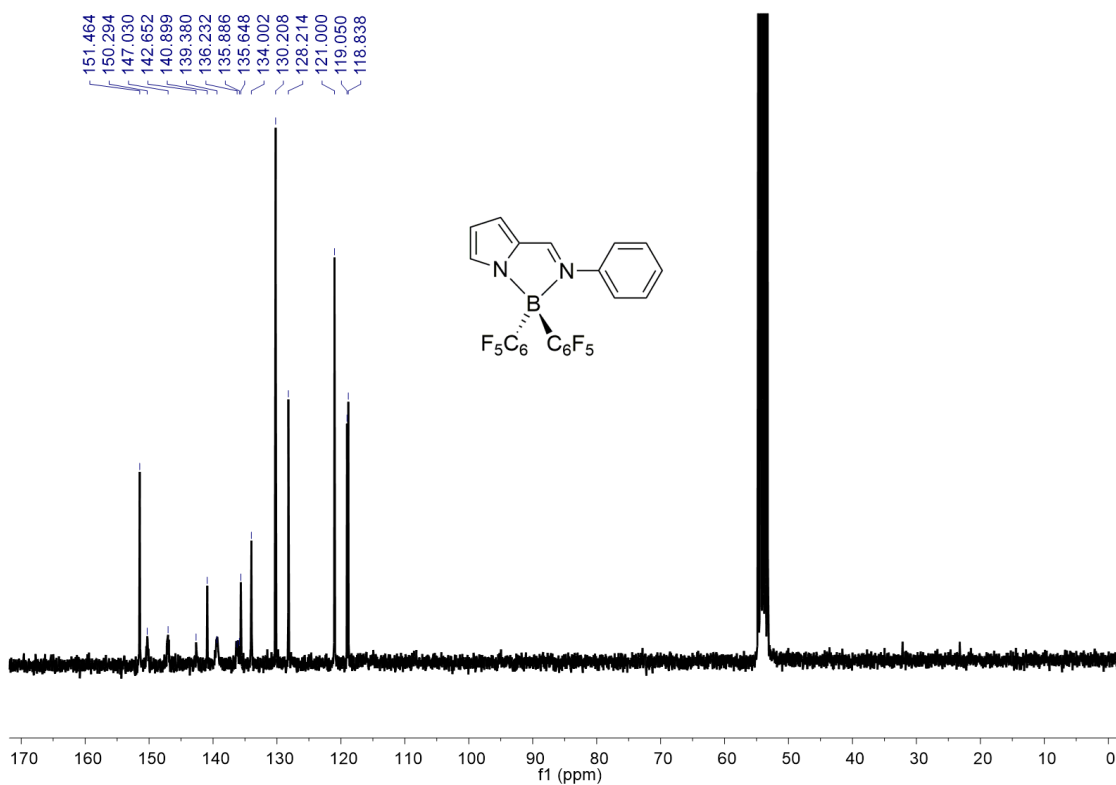


Figure S16. ¹³C{¹H} NMR spectrum (75.47 MHz, CD₂Cl₂) of complex 5.

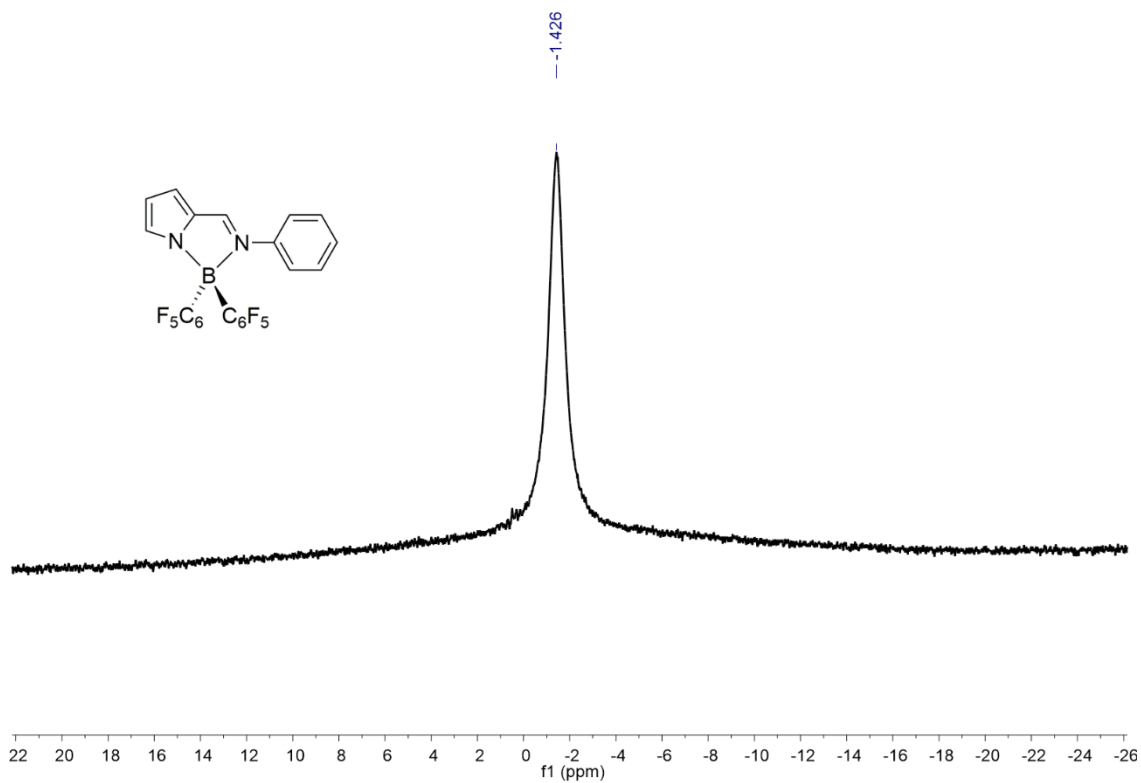


Figure S17. ^{11}B NMR spectrum (96.27 MHz, CD_2Cl_2) of complex **5**.

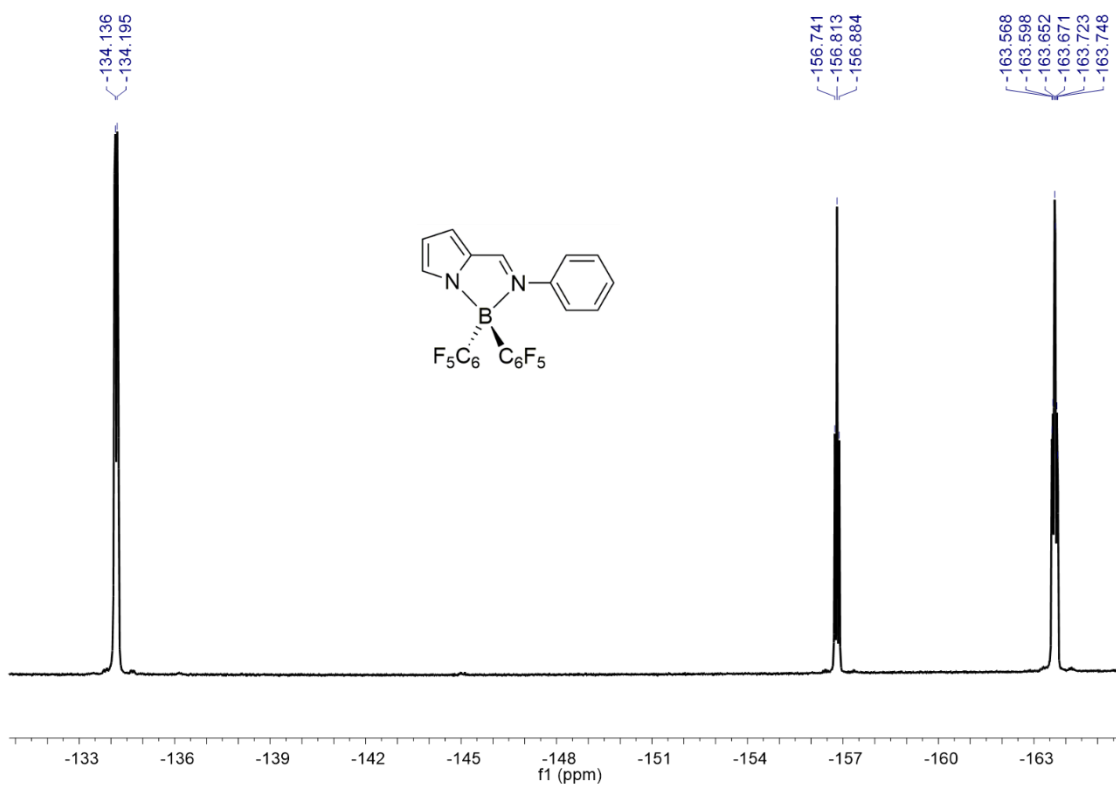


Figure S18. $^{19}\text{F}\{^1\text{H}\}$ NMR spectrum (282.40 MHz, CD_2Cl_2) of complex **5**.

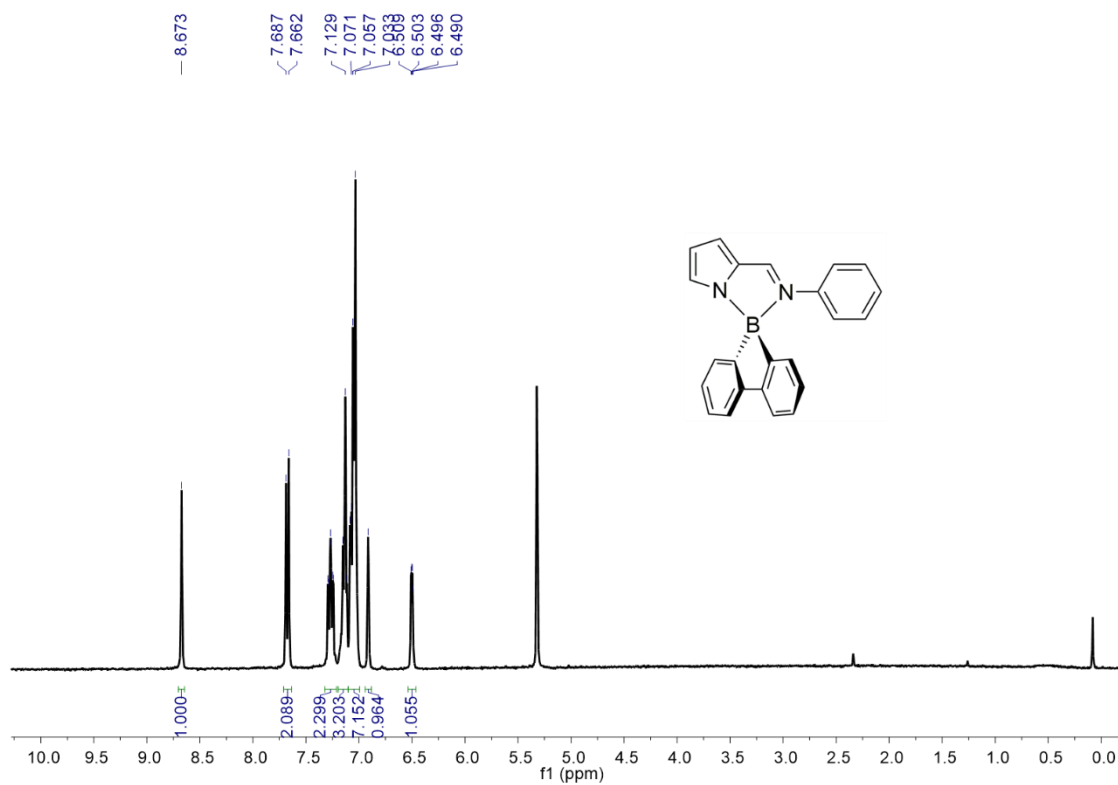


Figure S19. ^1H NMR spectrum (300 MHz, CD_2Cl_2) of complex **6**.

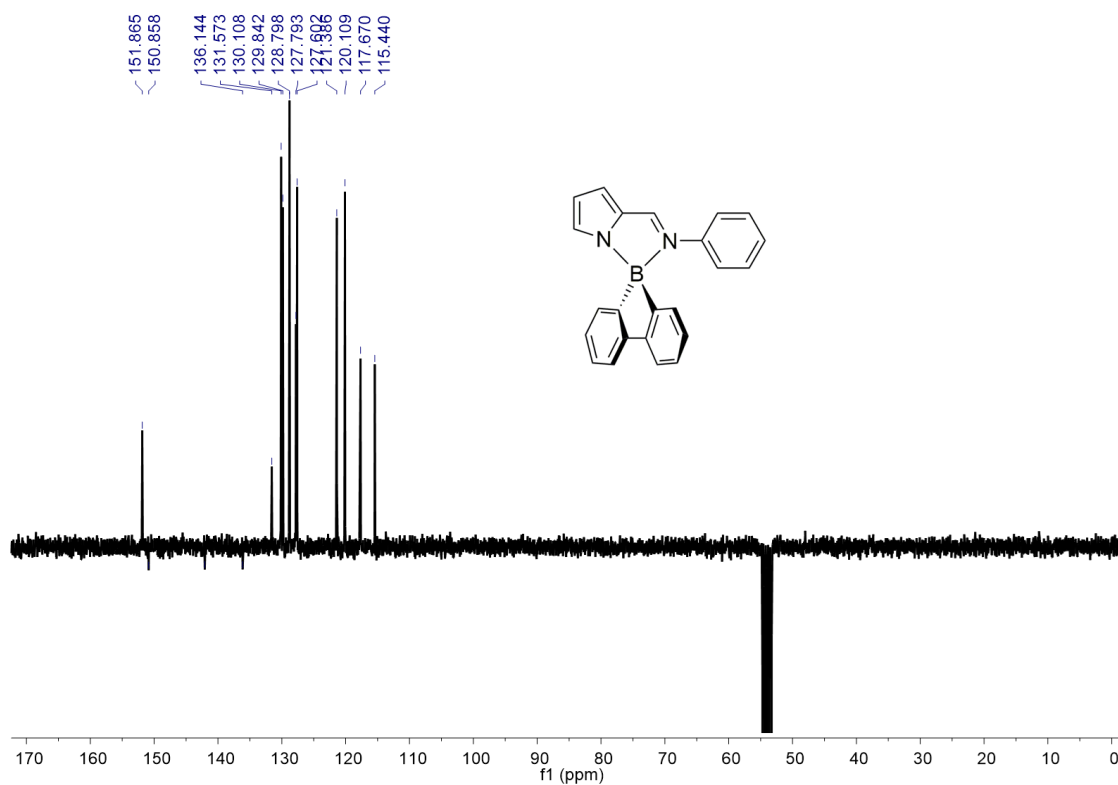


Figure S20. ^{13}C APT NMR spectrum (75.47 MHz, CD_2Cl_2) of complex **6**.

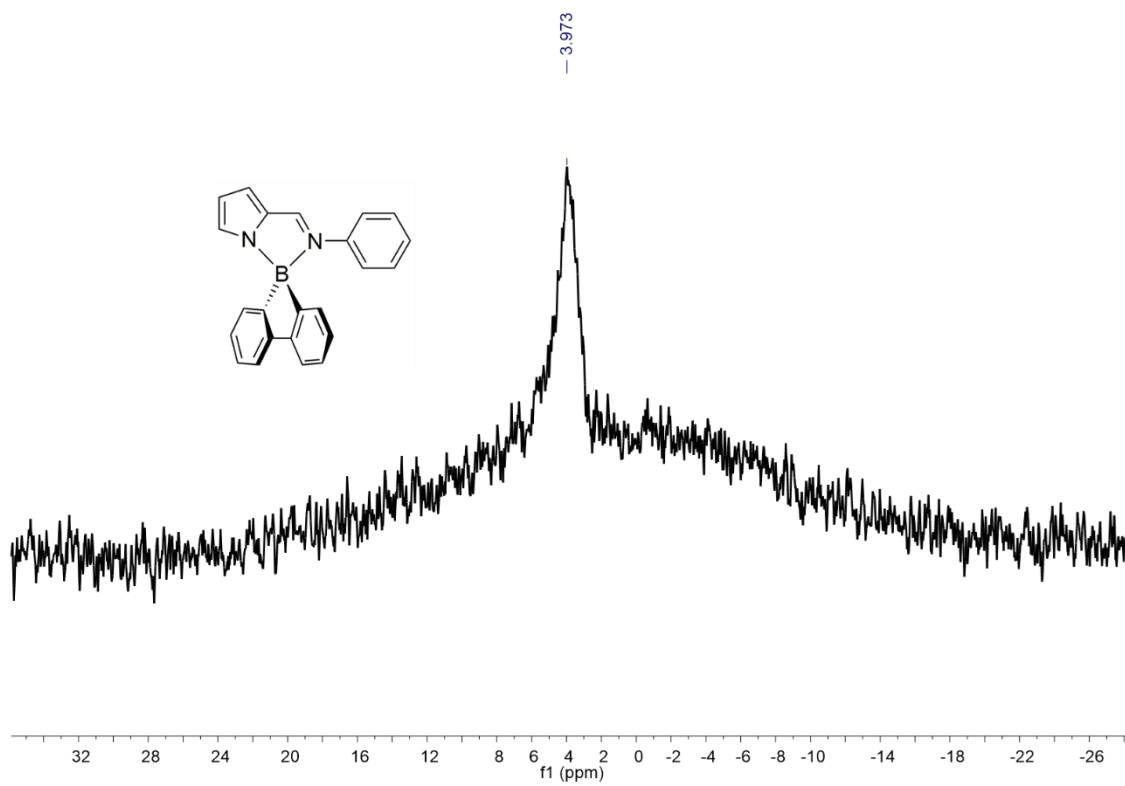


Figure S21. ^{11}B NMR spectrum (96.27 MHz, CD_2Cl_2) of complex **6**.

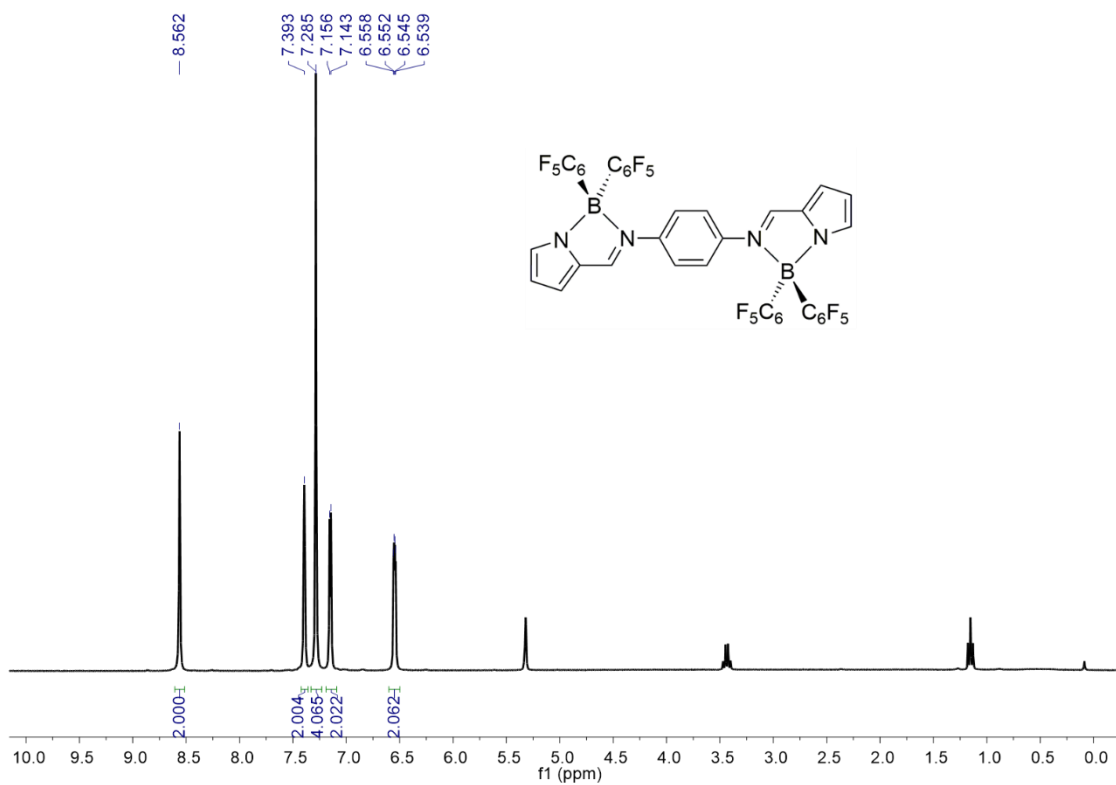


Figure S22. ^1H NMR spectrum (300 MHz, CD_2Cl_2) of complex 7.

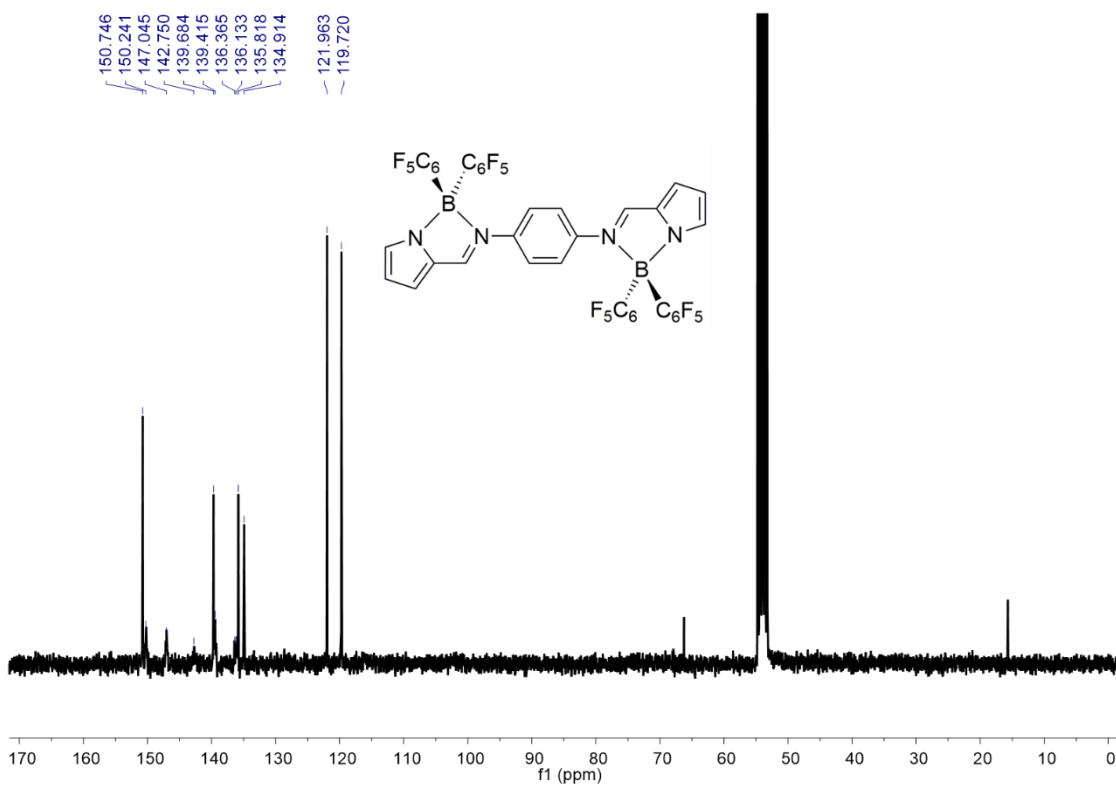


Figure S23. $^{13}\text{C}\{^1\text{H}\}$ NMR spectrum (75.47 MHz, CD_2Cl_2) of complex 7.

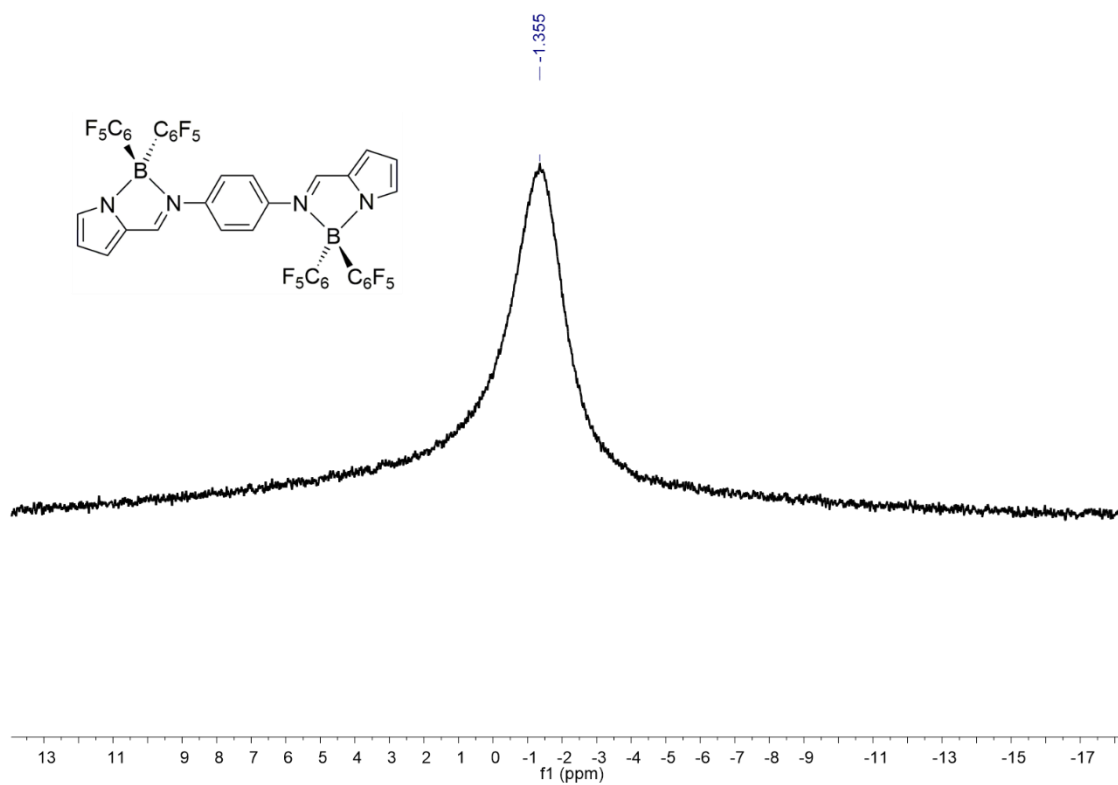


Figure S24. ^{11}B NMR spectrum (96.27 MHz, CD_2Cl_2) of complex **7**.

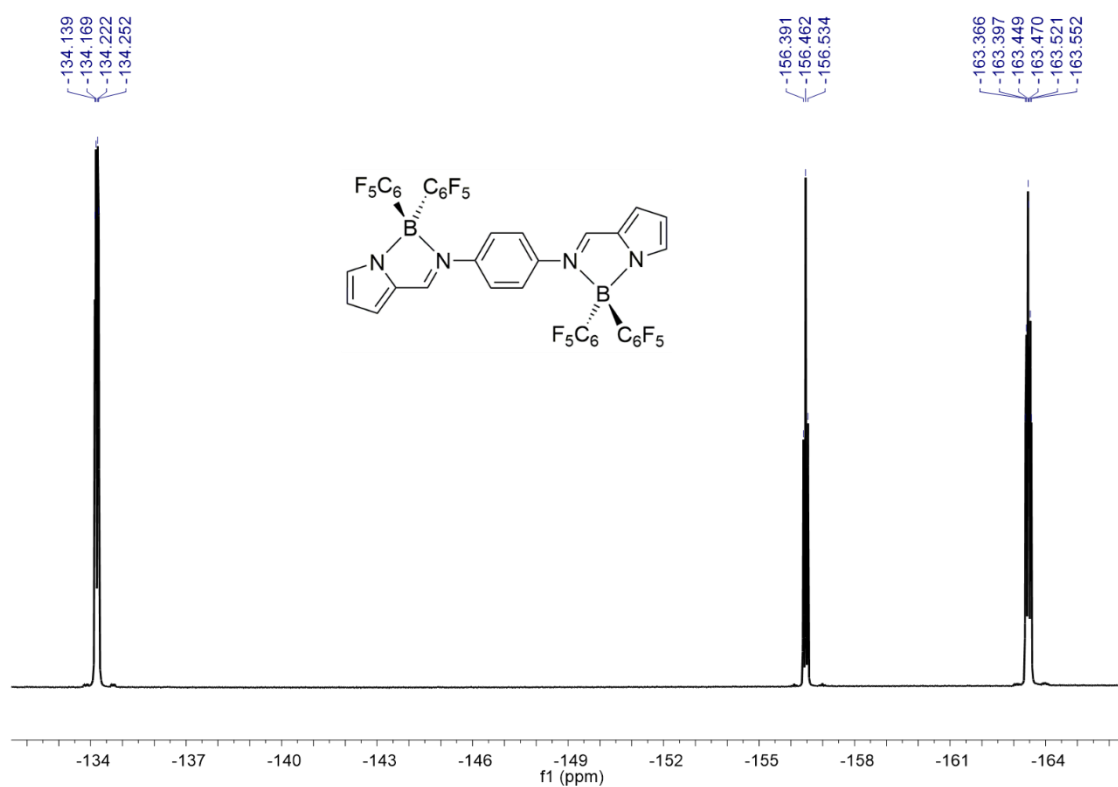


Figure S25. $^{19}\text{F}\{^1\text{H}\}$ NMR spectrum (282.40 MHz, CD_2Cl_2) of complex **7**.

Variable-temperature (VT) NMR spectra of complex **4**

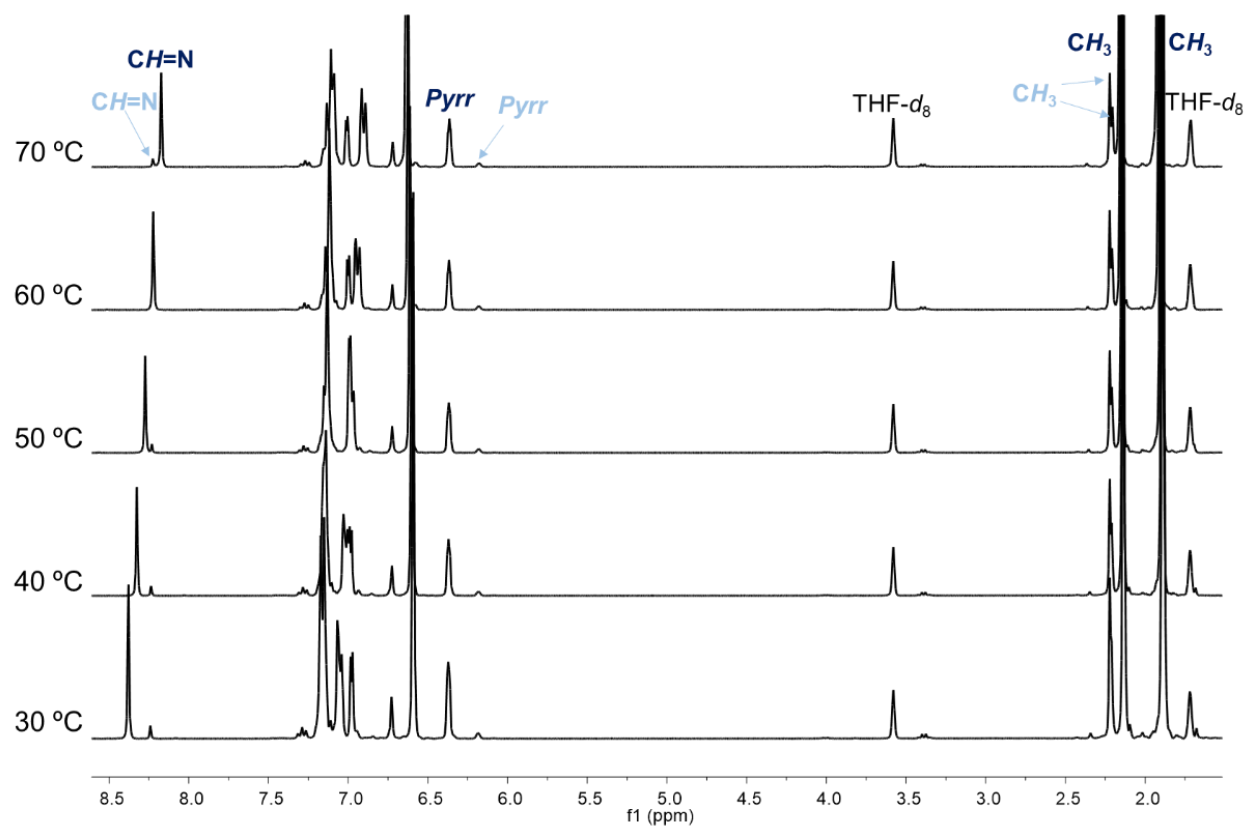


Figure S26. VT-¹H NMR spectra (300 MHz, THF-*d*₈) of complex **4**, showing the resonances of the tetracoordinate major isomer **4** (deep blue labels) and of the tricoordinate minor isomer **4**₃ (light blue labels).

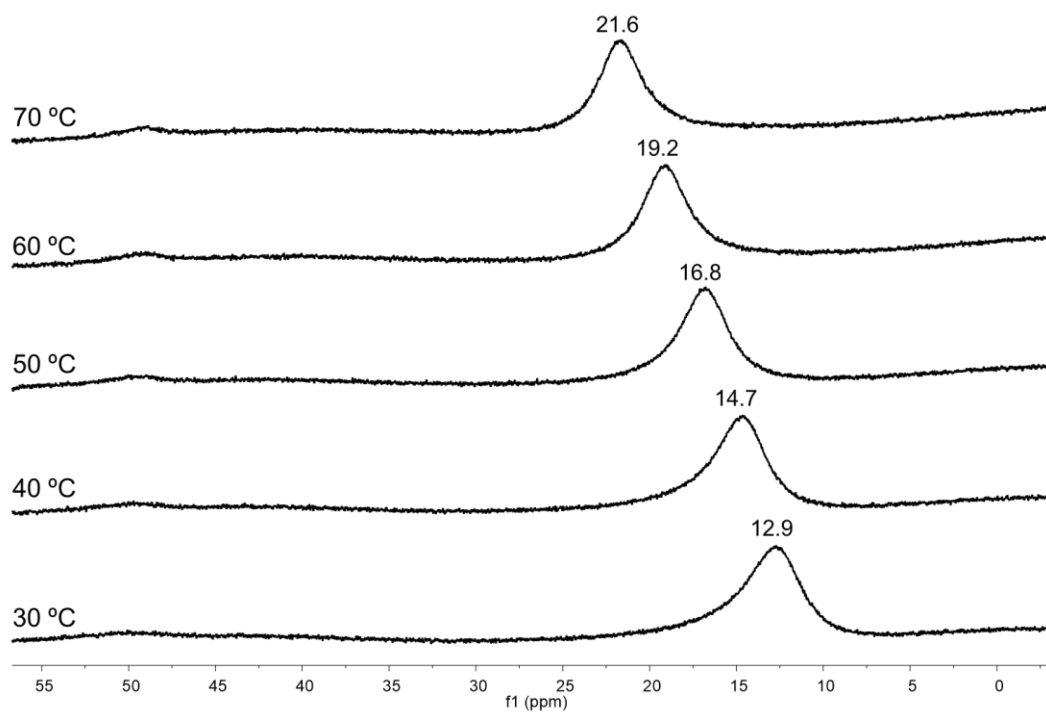


Figure S27. VT-¹¹B NMR spectra (96.29 MHz, THF-*d*₈) of complex **4**, showing the resonances of the tetracoordinate major isomer **4** (at lower fields) and the tricoordinate minor isomer **4**₃ (at higher fields), along with the respective chemical shifts.

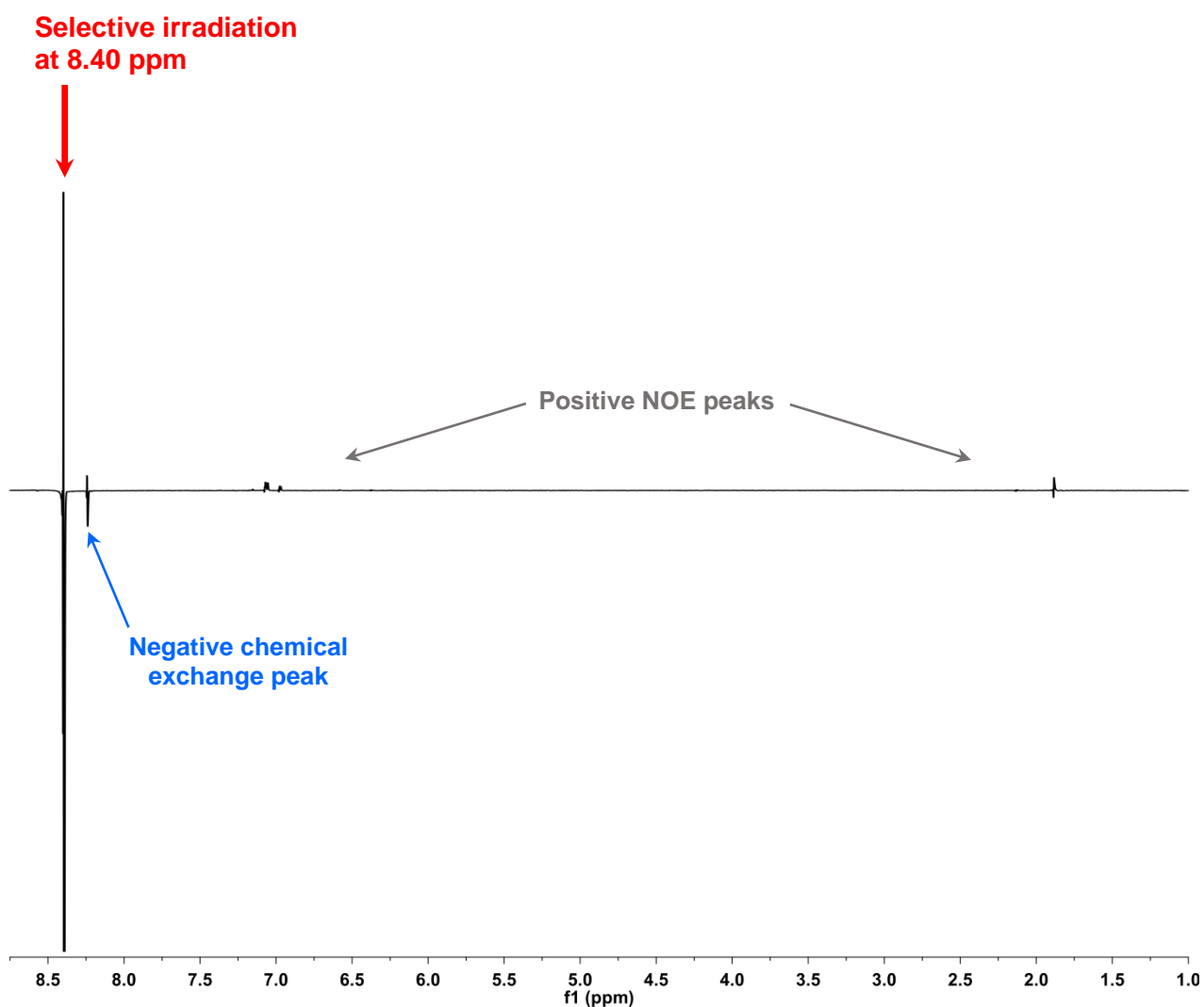


Figure S28. 1D-NOE NMR spectrum (300 MHz, THF-*d*₈, 29 °C) of complex **4**, with selective irradiation on the ¹H imine proton (-CH=N-) resonance of tetracoordinate major isomer **4**, at 8.40 ppm, showing its chemical exchange with the tricoordinate minor isomer **4**₃ (negative NOE peak) and positive NOE peaks with pyrrolyl, aromatic and methyl protons.

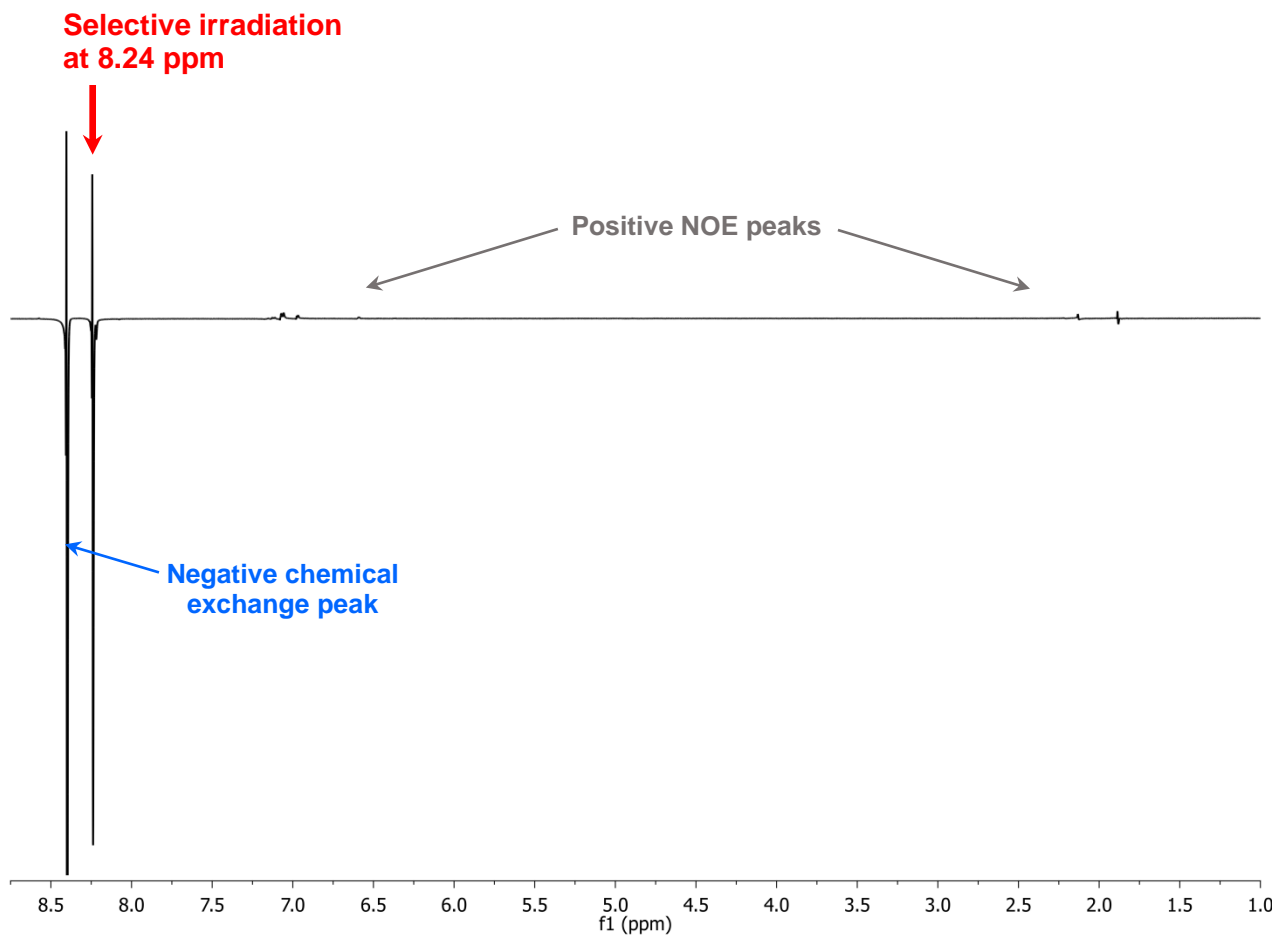


Figure S29. 1D-NOE NMR spectrum (300 MHz, THF-*d*₈, 29 °C) of complex **4**, with selective irradiation on the ¹H imine proton (-CH=N-) resonance of tricoordinate *minor isomer 4₃*, at 8.24 ppm, showing its chemical exchange with the tetracoordinate *major isomer 4* (negative NOE peak) and positive NOE peaks with pyrrolyl, aromatic and methyl protons.

Van't Hoff plot for the equilibrium between tetracoordinate and tricoordinate isomers of complex 4

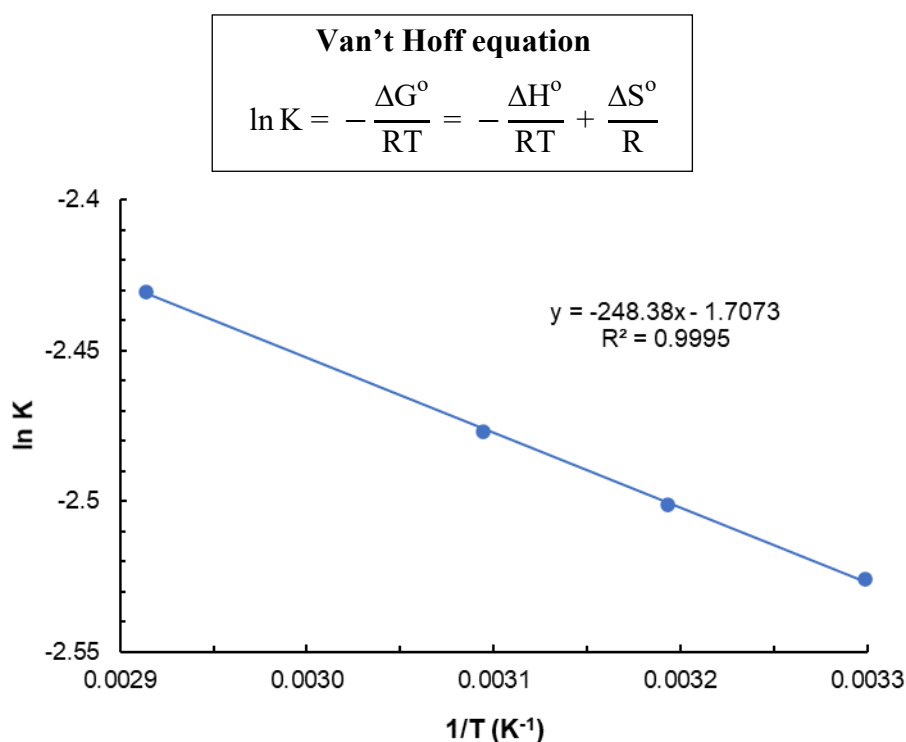


Figure S30. Van't Hoff plot for the equilibrium between tetracoordinate and tricoordinate isomers of complex 4.

T (°C)	T (K)	1/T	I _{tricoord} ^a	I _{tetracoord} ^a	K ^b
30	303.15	0.003299	0.080	1	0.080
40	313.15	0.003193	0.082	1	0.082
50	323.15	0.003095	0.084	1	0.084
60	333.15	0.003002	^c	1	^c
70	343.15	0.002914	0.088	1	0.088

^a Calculated from the relative area integration of the corresponding imine (-CH=N-) ¹H NMR resonances; ^b Equilibrium constant: K = [4₃]/[4] = I_{tricoord}/I_{tetracoord}; ^c Not calculated because both resonances are overlapping.

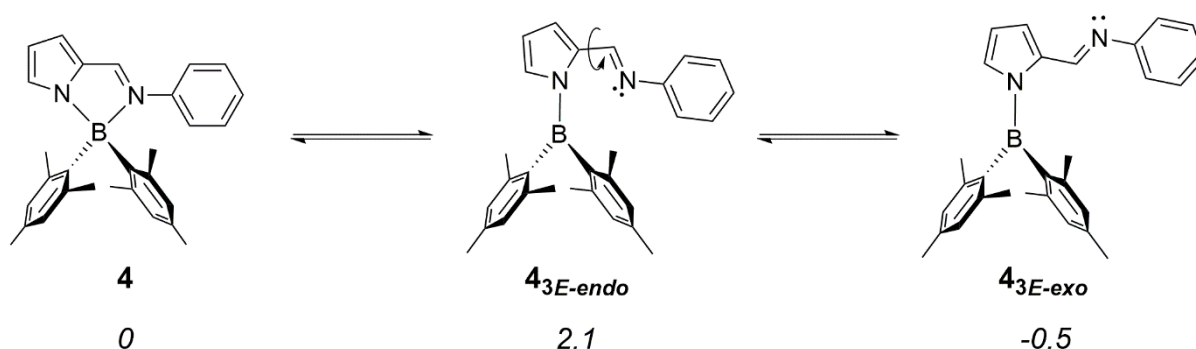
Thermodynamic parameters: $\Delta H^\circ = 0.49 \pm 0.04 \text{ kcal mol}^{-1}$

$\Delta S^\circ = -3.4 \pm 0.1 \text{ cal mol}^{-1} \text{ K}^{-1}$

$\Delta G^\circ (298.15 \text{ K}) = 1.51 \pm 0.07 \text{ kcal mol}^{-1}$

Computational studies – Energy profile for the conversion of complex **4 into the tricoordinate isomers **4**_{3E-endo} and **4**_{3E-exo} and comparison with mononuclear boron complexes **3**, **5**, **6** and **8****

It was shown in Scheme 2 of the article that the tetracoordinate 2-iminopyrrolyl boron complex **4** was involved in an equilibrium with the **4**_{3E-endo} isomer, which could further convert to **4**_{3E-exo}. Our calculations indeed show that the B-N_{imine} bond of complex **4** can be easily broken to yield a tricoordinate boron complex containing the monodentate iminopyrrolyl ligand in the *E-endo* form (**4**_{3E-endo}) with an energy 2.1 kcal mol⁻¹ higher. Rotation around the C_{pyrrolyl}-C_{imine} converts it to a 2.6 kcal mol⁻¹ more stable *E-exo* conformer (**4**_{3E-exo}) with almost the same energy of **4**, though slightly more stable. A new version of Scheme 2 with these energies is shown in Scheme S1.



Scheme S1. Schematic equilibrium between the tetracoordinate 2-iminopyrrolyl boron complex **4** and its tricoordinate isomers **4**_{3E-endo} and **4**_{3E-exo}, with their relative energies in kcal mol⁻¹ (in italics).

This result suggests that the long B-N_{imine} bond is weak, and its cleavage relieves the steric hindrance of the initial complex **4**. Nothing similar happens with the other four mononuclear complexes studied, where the energy differences are closer to 20 kcal mol⁻¹ (see Figure S31). The **6**_{3E-endo} isomer of **6** could not be obtained. Therefore, only tetracoordinate complex **4** may be involved in a decoordination-coordination equilibrium process in solution with its corresponding tricoordinate species as represented in Scheme S1.

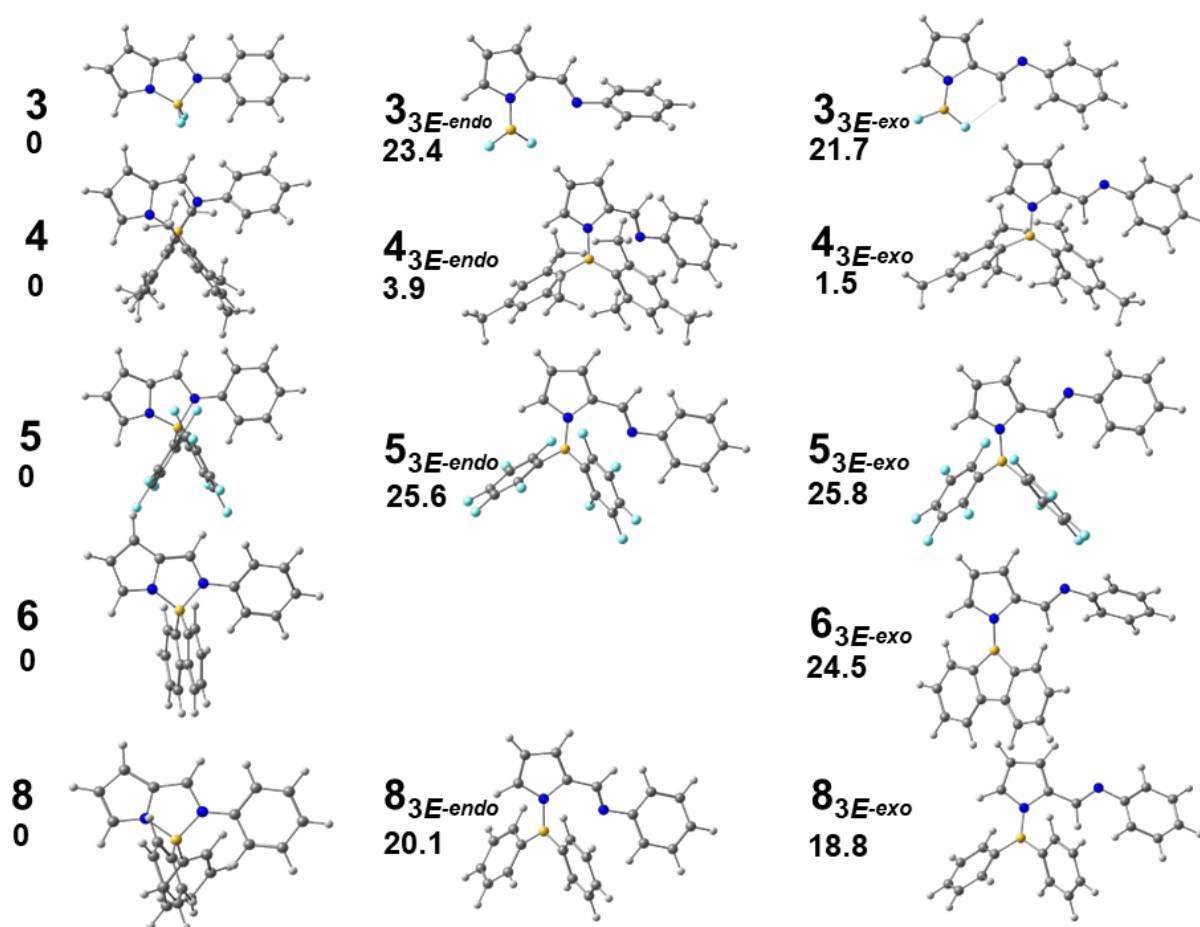


Figure S31. Optimised ground state structures of tetracoordinate mononuclear boron complexes **3-6** and **8** (left), of their tricoordinate *E-endo* conformers (center, except $6_{3E-endo}$) and tricoordinate *E-exo* conformers (right), with the relative energy difference (kcal mol⁻¹) below the complex label.

The previous observations led us to search for the energy profile of **4**, $4_{3E-endo}$ and 4_{3E-exo} (bottom) of the two reactions shown in Scheme S1 and to determine the two transition states, TS1 and TS2, respectively (see Computational details for the methodology). The description of the mechanism is presented in Figure S30 (displayed in the article as Figure 2, which is repeated here for facility).

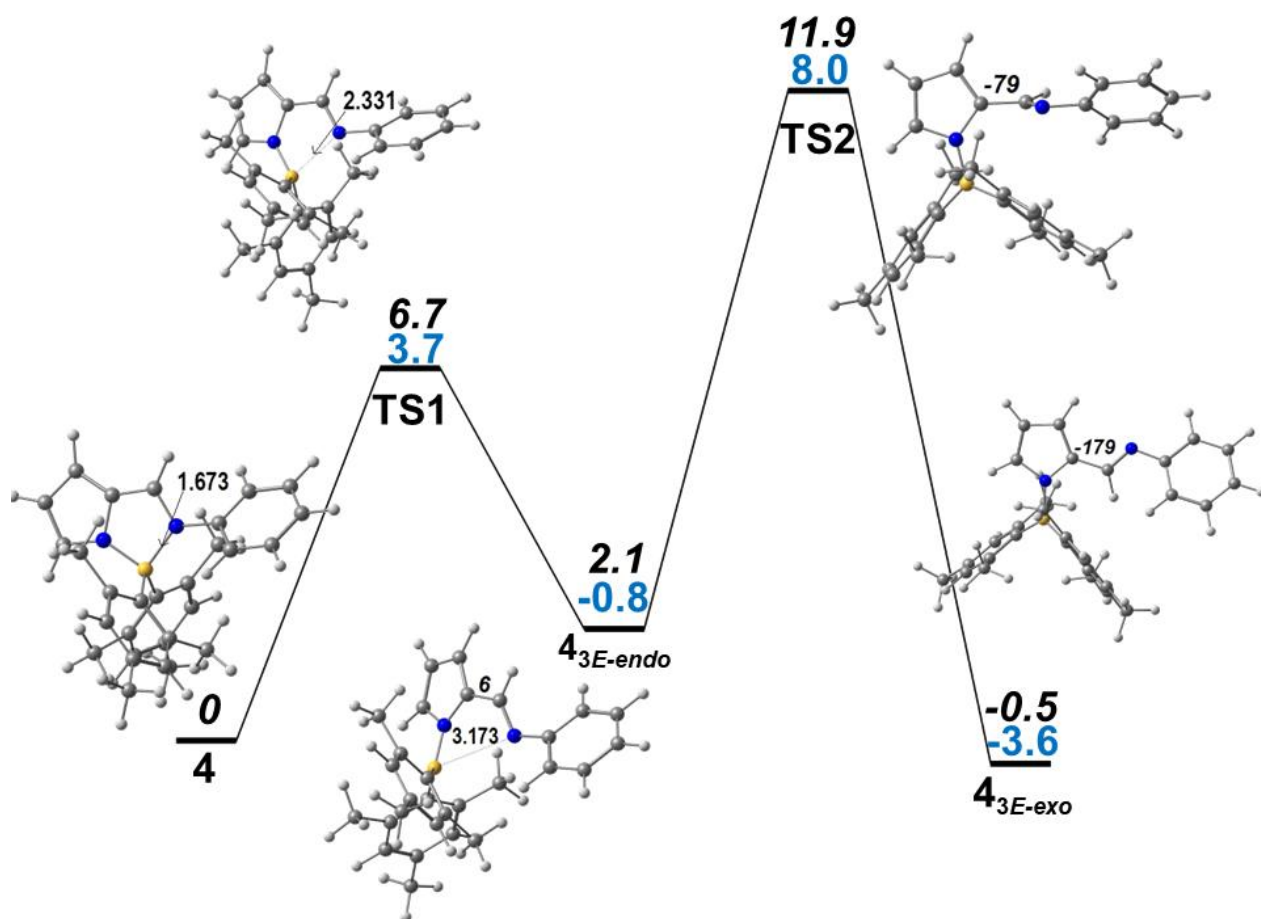


Figure S32. Energy profile (BP86 functional) for the conversion of complex **4** into the tricoordinate complex **4_{3E-endo}** and isomerization to **4_{3E-exo}** (bottom), with the relative energies (black) and Gibbs energies (blue) in kcal mol⁻¹, and the geometries of the five species with indication of the parameter changing in each step (distances in Å in TS1 and C-C-C-N dihedral angles in ° in TS2).

The stretching of the B-N_{imine} bond of **4** shows an energy maximum, which led to the transition state at a distance of 2.331 Å and to the tricoordinate boron complex **4_{3E-endo}** for d(B-N_{imine}) = 3.173 Å, which is well beyond any bonding distance. The small energy barrier is 6.7 kcal mol⁻¹. If we consider the Gibbs energies values, the tetra- and tricoordinate boron complexes differ by only 0.8 kcal mol⁻¹, the latter becoming more stable than **4**. It is therefore expectable that both species **4** and **4_{3E-endo}** could be seen in solution by NMR experiments, as discussed above. While looking for meaningful species, we envisaged also the **4_{3E-exo}** isomer, which is obtained by rotating the -C(H)=N-Ph imine group across the internal C_{pyrrolyl}-C_{imine} bond of the iminopyrrolyl. This angle starts as 2° in **4**, with the C=N imine bond almost coplanar with the pyrrolyl ring and is only 6° in **4_{3E-endo}**, reaching -79° in TS2 and finally -179° in **4_{3E-exo}**. The C=N imine bond of **4_{3E-exo}** is again coplanar with the pyrrolyl

ring but in the *exo* conformation. The energy barrier is significantly higher and may prevent its formation. These values are very small, and the conclusion is that both **4** and **4**_{3E-endo} should be observed species. The presence of **4**_{3E-exo} is not so clear.

This latter point is further reflected in the similar calculations obtained with another methodology (Figure S33). A comparison of experimental and calculated thermodynamic functions for the equilibrium between **4** and **4**_{3E-endo} reveals that the enthalpies are in very good agreement, with 0.6 (calc) and 0.5 (exp) kcal mol⁻¹, while the Gibbs energies, -0.8 (calc) and 1.5 (exp) kcal mol⁻¹ differ a little more, though being of the same order of magnitude. This not so good agreement is explained by the limitations in the calculations of the entropy.

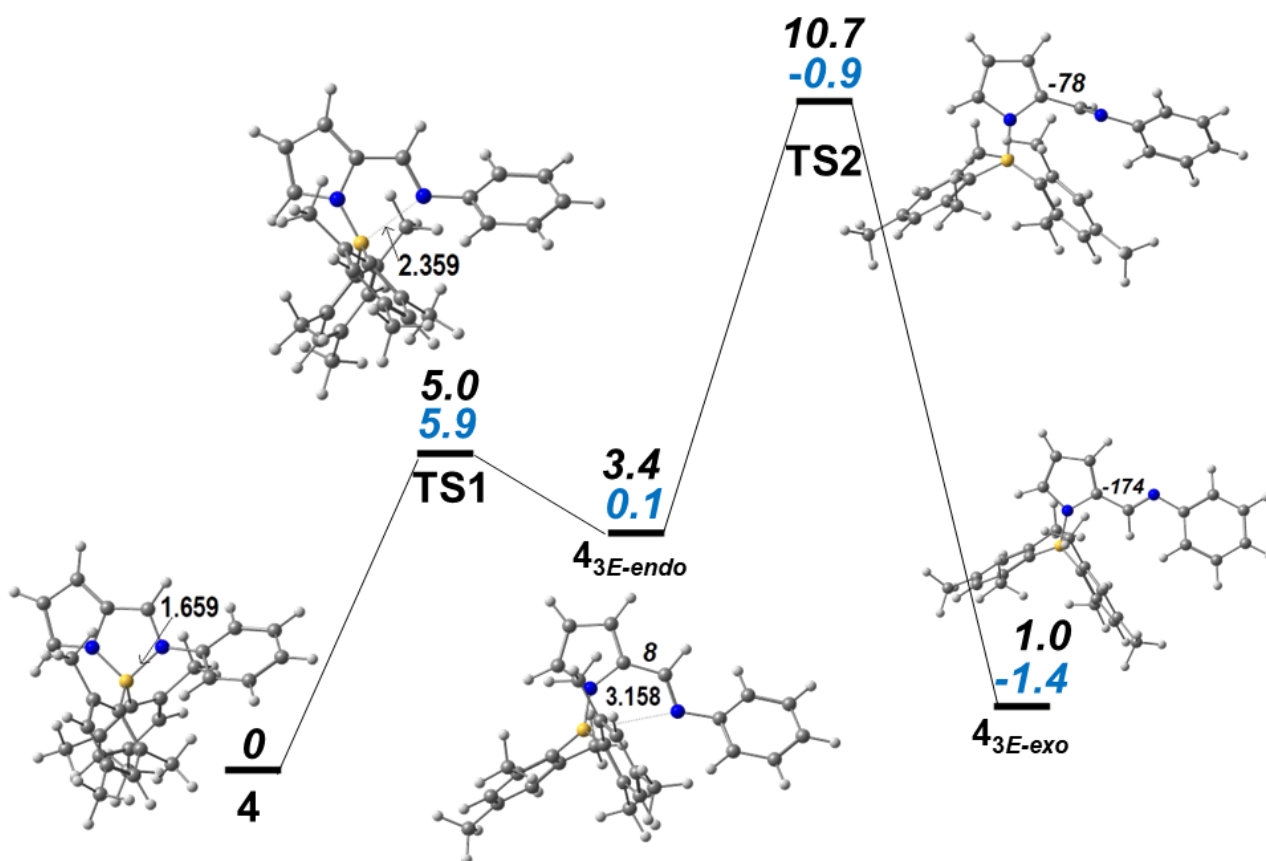


Figure S33 Energy profile (PBE functional) for the conversion of complex **4** into the tricoordinate complex **4**_{3E-endo} and isomerization to **4**_{3E-exo} (bottom), with the relative energies (black) and Gibbs energies (blue) in kcal mol⁻¹, and the geometries of the five species with indication of the relevant parameters (angles in ° and distances in Å).

**Computational studies – Ground state and first excited state optimised structure geometries
of boron complexes 3-9**

Table S4. Calculated (DFT) dihedral angles C6-N2-C7-C12 (°) for complexes **3-9** in the ground and first singlet excited state using different methods.

Angle	Ground state					First singlet excited state				
	A	B	A/D3	B/D3	GP	A	B	A/D3	B/D3	GP
	C6-N2-C7-C12									
3	-24	-27	-25	-28	-22	1	0	1	0	0
4	-49	-51	-53	-56	-48	13	13	14	15	9
5	23	25	23	24	23	8	8	8	8	9
6	30	33	30	29	30	5	5	5	5	0
7	22	24	21	23	22	10	11	10	11	10
	-22	-25	-21	-23	-21	-9	-11	-10	-11	-10
8	36	36	36	38	29	1	1	1	1	2
9	31	37	31	37	34	5	4	5	5	4
	-31	-37	-31	-37	-34	-5	-5	-5	-5	-4

A – PBE0, TZ2P (all electron), THF, SO

A/D3 – PBE0/D3, TZ2P (all electron), THF, SO

B – B3LYP, TZ2P (all electron), THF, SO

B/D3 – B3LYP/D3, TZ2P (all electron), THF, SO

GP – BP86 (small core, TZ2P)

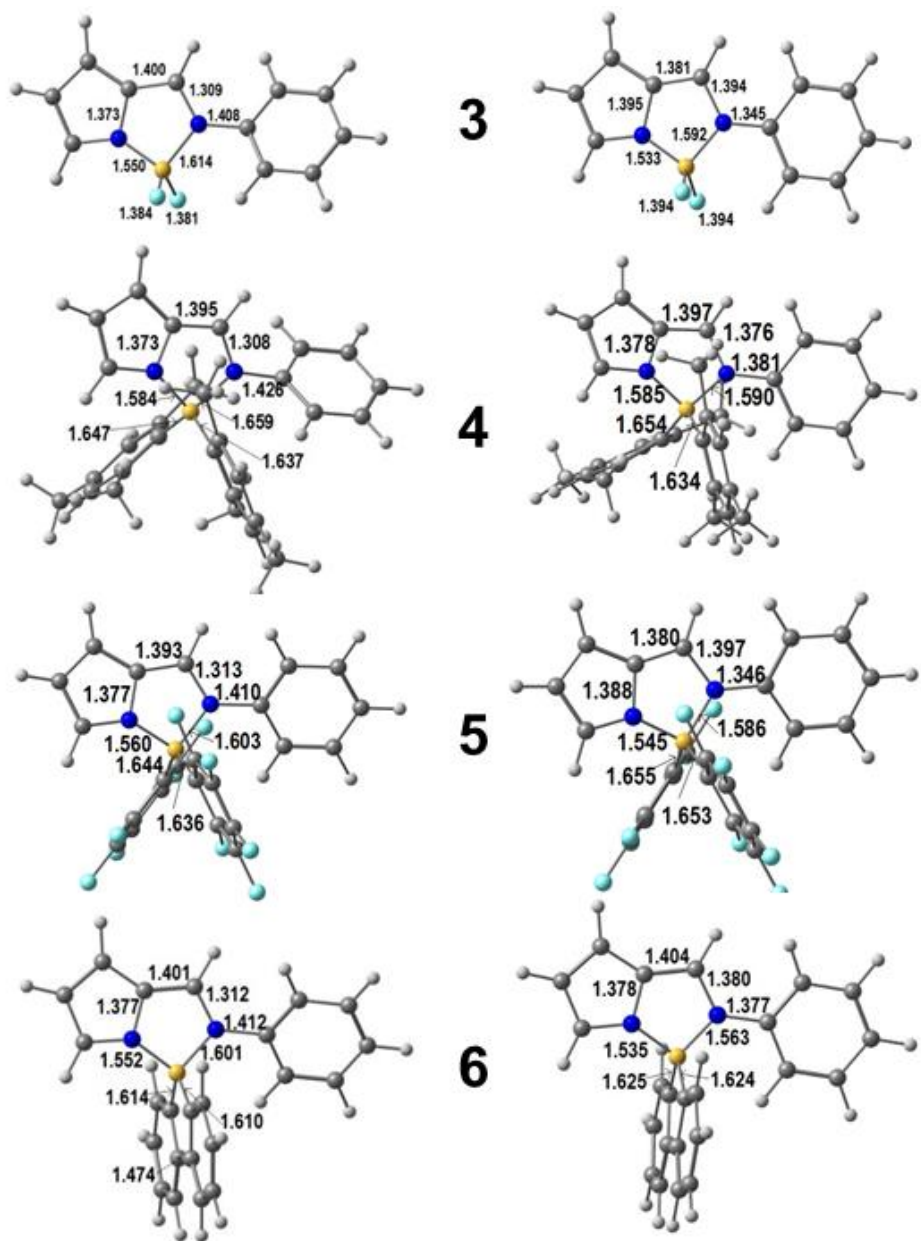


Figure S34. Optimised structures of tetracoordinate boron complexes **3-6** in the ground state (left) and in the first excited singlet state (right), with the most relevant distances (Å).

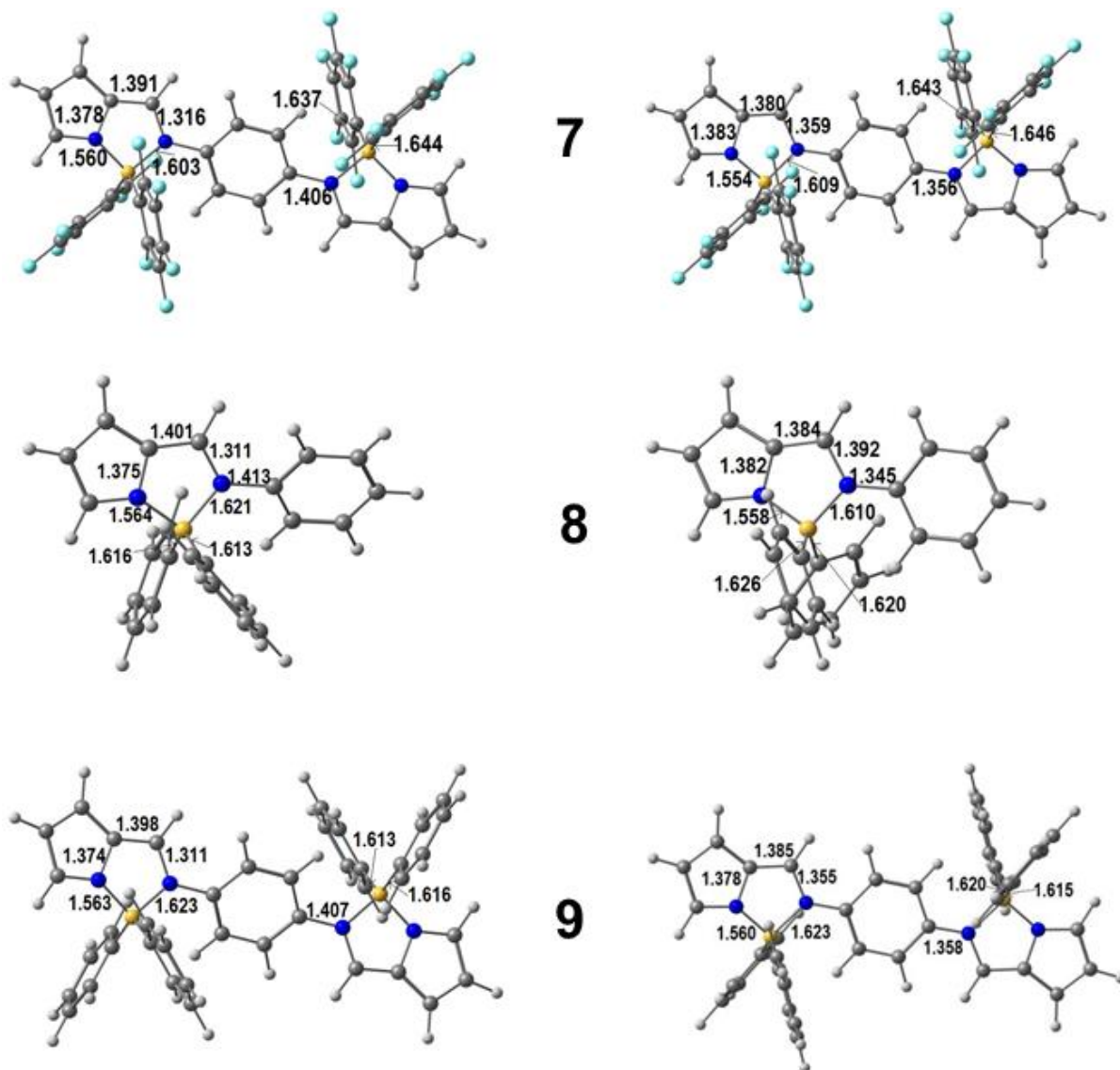


Figure S35. Optimised structures of tetracoordinate boron complexes **7-9** in the ground state (left) and in the first excited singlet state (right), with the most relevant distances (Å).

Computational studies – Frontier orbitals and composition of the lower energy electronic transitions in boron complexes **4** and **6**

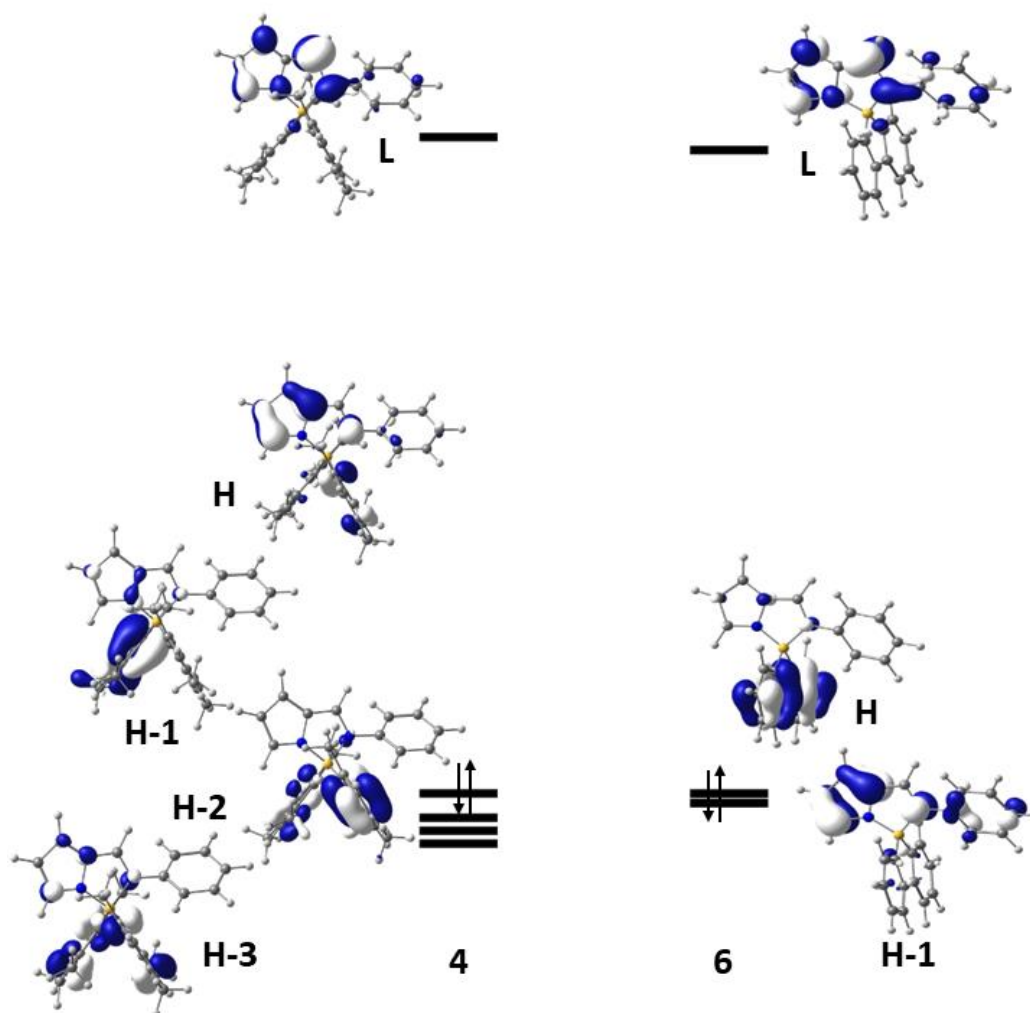


Figure S36. Three-dimensional representation of the frontier orbitals of mononuclear complexes **4** and **6** with relative energies (HOMO-LUMO gap: 4.24 (**4**), 3.71 (**6**) eV; the HOMO is identified by the arrows).

Computational studies – Calculated HOMOs and LUMOs energies for complexes 3-9 using different methods

Table S5. Calculated HOMOs and LUMOS energies (eV) for complexes **3-9** using different methods.

	A		A/D3		B		B/D3		GP		THF		CH ₂ Cl ₂	
	HOMO	LUMO	HOMO	LUMO	HOMO	LUMO	HOMO	LUMO	HOMO	LUMO	HOMO	LUMO	HOMO	LUMO
3	-6.490	-2.443	-6.488	-2.441	-6.184	-2.489	-6.182	-2.485	-5.722	-3.390	-5.540	-3.143	-5.632	-3.243
4	-6.277	-2.033	-6.268	-2.014	-5.959	-2.068	-5.944	-2.045	-5.342	-2.978	-5.373	-2.827	-5.424	-2.886
5	-6.532	-2.470	-6.526	-2.472	-6.230	-2.522	-6.219	-2.526	-5.880	-3.519	-5.617	-3.188	-5.691	-3.263
6	-6.249	-2.156	-6.249	-2.158	-5.899	-2.179	-5.897	-2.180	-5.251	-3.082	-5.440	-2.944	-5.445	-2.987
7	-6.335	-2.793	-6.320	-2.800	-6.057	-2.822	-6.034	-2.832	-5.830	-3.900	-5.442	-3.459	-5.509	-3.521
8	-6.355	-2.097	-6.352	-2.095	-6.038	-2.145	-6.040	-2.124	-5.396	-2.933	-5.414	-2.877	-5.511	-2.978
9	-6.133	-2.410	-6.129	-2.424	-5.876	-2.392	-5.869	-2.392	-5.224	-3.213	-5.201	-3.123	-5.309	-3.232

A – PBE0, TZ2P (all electron), THF, SO

A/D3 – PBE0/D3, TZ2P (all electron), THF, SO

B – B3LYP, TZ2P (all electron), THF, SO

B/D3 – B3LYP/D3, TZ2P (all electron), THF, SO

GP – BP86 (small core, TZ2P)

THF – BP86 (small core, TZ2P), THF (single point)

CH₂Cl₂ – BP86 (small core, TZ2P), dichloromethane (single point)

Computational studies – Calculated absorption energies and first excited state lifetimes for complexes 3-9 using different methods

Table S6. Calculated absorption energies (eV) and first excited state lifetimes (ns) for complexes **3-9** using different methods.

	A		A/D3		B		B/D3		GP
	λ_{abs}^{max}	τ_f	λ_{abs}^{max}	τ_f	λ_{abs}^{max}	τ_f	λ_{abs}^{max}	τ_f	λ_{abs}^{max}
3	3.36	1.94	3.36	1.97	3.29	2.13	3.29	2.13	2.16
4	3.79	7.24	3.80	15.0	3.72	11.2	3.80	14.47	3.39
5	3.41	2.02	3.40	2.03	3.33	2.17	3.32	2.19	3.14
6	3.50	1.80	3.50	1.83	3.46	1.85	3.41	1.87	3.29
7	2.88	1.59	2.86	1.61	2.80	1.80	2.77	1.82	2.39
8	3.45	1.84	3.59	1.77	3.39	1.94	3.54	1.87	3.29
9	3.04	1.41	3.04	1.42	3.03	1.57	3.03	1.58	2.47

A – PBE0, TZ2P (all electron), THF, SO

A/D3 – PBE0/D3, TZ2P (all electron), THF, SO

B – B3LYP, TZ2P (all electron), THF, SO

B/D3 – B3LYP/D3, TZ2P (all electron), THF, SO

GP – BP86 (small core, TZ2P)

Computational studies – Composition of the lower energy electronic transitions in complexes 4 and 6

Table S7. Composition and oscillator strength (OS) of the lower energy electronic transitions in complexes 4 and 6.

Transition	λ (nm)	E (eV)	Composition	OS
Complex 4				
1	352	3.52	H→L (56%), H-1→L (36%)	0.107
2	347	3.57	H-1→L (62%), H→L (27%)	0.251
3	331	3.75	H-2→L (89%), H→L (8%)	0.150
4	317	3.91	H-3→L (90%), H→L (5%)	0.448
Complex 6				
1	374	3.31	H→L (96%)	0.033
2	354	3.50	H-1→L (94%), H→L (3%)	1.039

Computational studies – Calculated energies of $S_1 \rightarrow S_0$ transition for complexes 3-9 using different methods

Table S8. Calculated energies (eV) of $S_1 \rightarrow S_0$ transition for complexes **3-9** using different methods.

	S_1				
	A	B	A/D3	B/D3	GP
3	2.57	2.476	2.56	2.45	1.80
4	2.37	2.21	2.35	2.15	1.815
5	2.64	2.53	2.64	2.60	1.87
6	2.57	2.37	2.57	2.35	2.09
7	2.25	2.17	2.26	2.17	1.52
8	2.70	2.60	2.70	2.60	1.89
9	2.55	2.15	2.55	2.45	1.50

A – PBE0, TZ2P (all electron), THF, SO

A/D3 – PBE0/D3, TZ2P (all electron), THF, SO

B – B3LYP, TZ2P (all electron), THF, SO

B/D3 – B3LYP/D3, TZ2P (all electron), THF, SO

GP – BP86 (small core, TZ2P)

Electrochemical properties

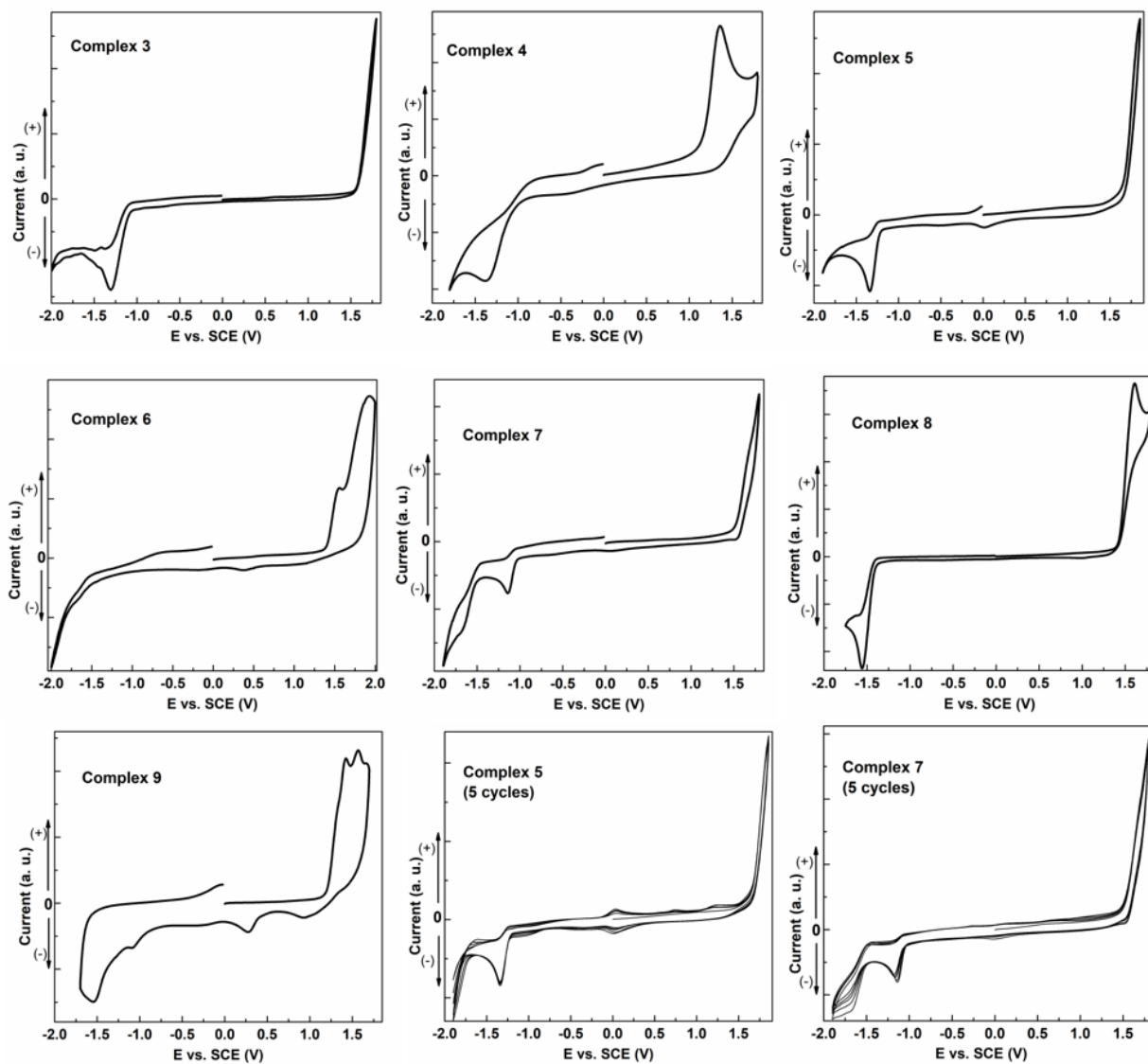
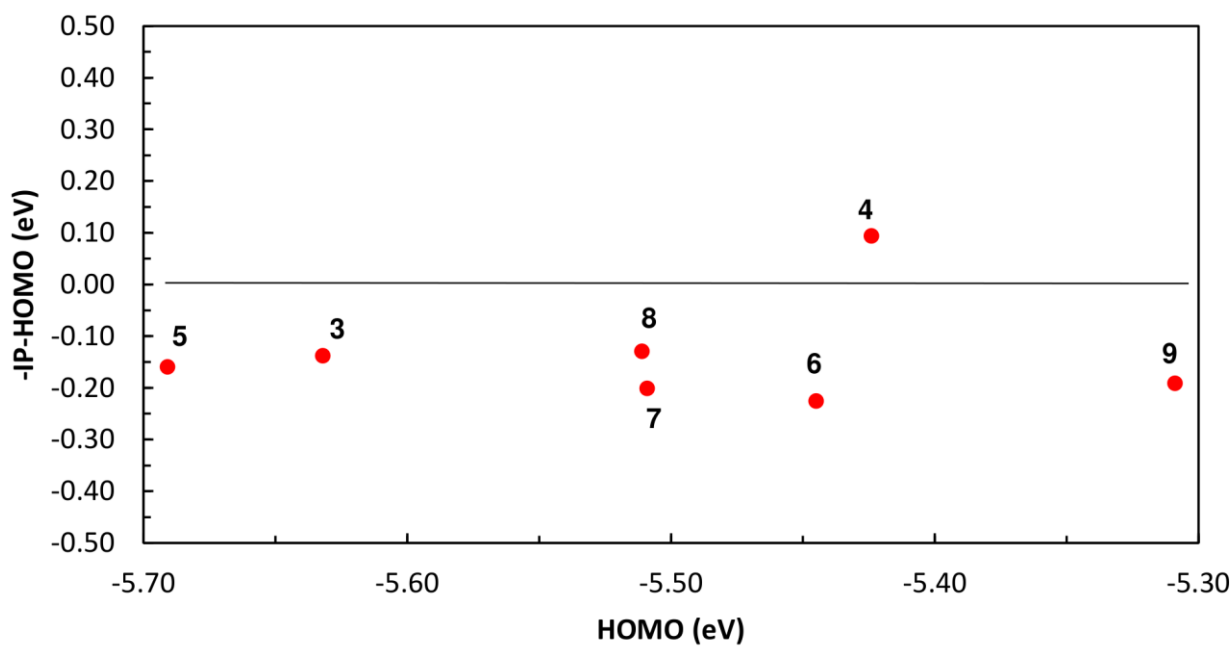
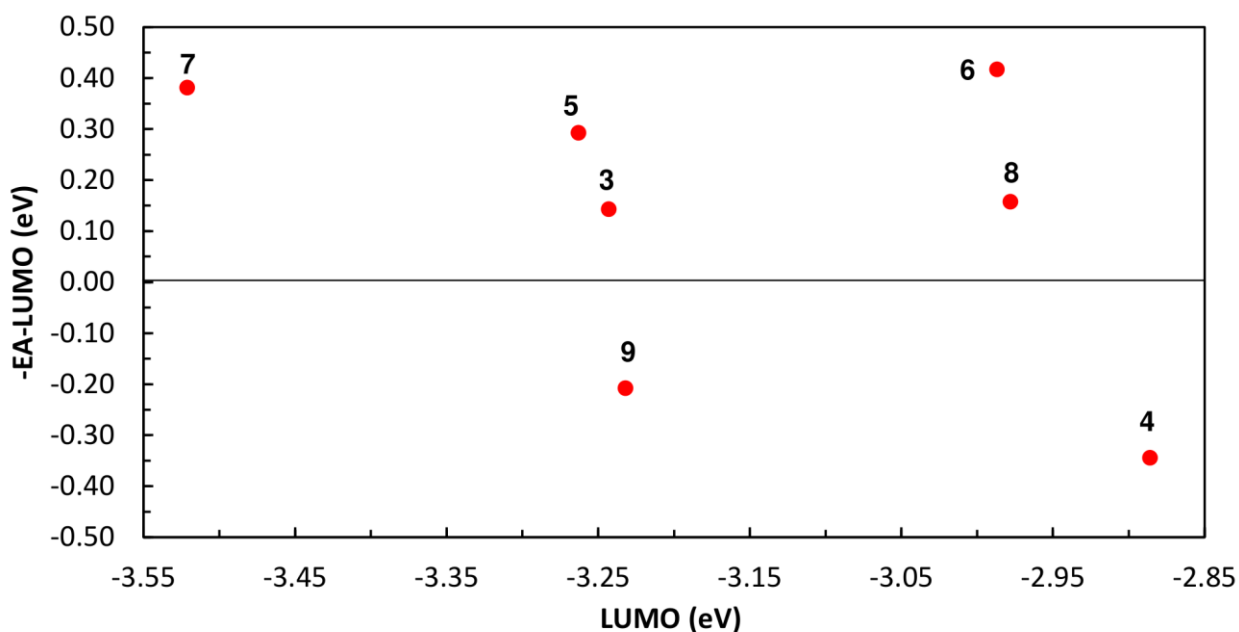


Figure S37. Cyclic voltammograms obtained for complexes **3-9** in this work, measured at scan rate of 50 mV/s in 0.1 M TBABF₄/CH₂Cl₂ (for complexes **3-8**) or 0.1 M TBAClO₄/CH₂Cl₂ (for complex **9**) as electrolytes.



(a)



(b)

Figure S38. Plots of (a) the difference between $-IP$ and HOMO versus the energies of the HOMOs, and of (b) the difference between $-EA$ and LUMO versus the energies of the LUMOs of compounds **3–9**. IP and EA were estimated from cyclic voltammetry measurements, and the energies of the HOMOs and LUMOs were determined by DFT (CH_2Cl_2).

Electroluminescence performance

Table S8 summarises the performance parameters of the various OLEDs fabricated with the new complexes deposited by spin coating. It also includes the previously reported results for the OLEDs based on neat **8** and **9**.

OLEDs based on neat complexes **3** and **4** showed negligible emission, a result consistent with the low or null photoluminescence (PL), and were not further investigated. Devices based on neat complex **5** showed also negligible emission. In view of the reasonable PL efficiency this was further studied in OLEDs upon dispersion in polyvinylcarbazole (PVK).

We also observed that films of neat complex **7** showed signs of crystallization, leading to rough surfaces.

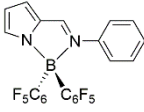
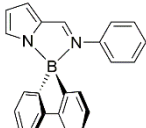
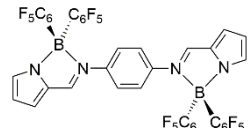
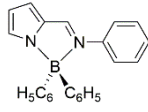
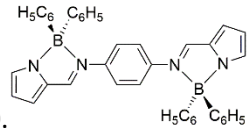
Figure S39 compares the recorded EL spectra for neat complexes and for the complexes dispersed in PVK with the corresponding PL spectra. A good agreement is observed. Small differences are likely due to interference effects inside the OLEDs (which resemble a microcavity). No additional peaks are observed in EL that could result from degradation or from lower energy emissive states (such as aggregates).

In view of the close molecular structure of complexes **7** and **9**, the similar solution fluorescence quantum yield, and the above mentioned tendency of crystallization of complex **7** films, we investigated the performance of OLEDs based on a 1:1 weight mixture of the two complexes. The devices had the structure ITO/PEDOT:PSS/**7+9**/Ca/Al, with a pixel area of 8 mm² and the active layer thickness (**7+9**) of *ca.* 60 nm. Figure S40 compares the performance of these devices with those of the neat complexes.

We found that the OLEDs combining the two complexes do not outperform that of the OLEDs based on neat **9**. The typical maximum luminance of the OLEDs based on the **7+9** mixture, 27 cd m⁻², is lower than those of the OLEDs based on neat **7** (43 cd m⁻²) or **9** (958 cd m⁻²), and the current efficiency (as shown in Fig S40B) is slightly higher than that of neat **7**-based OLEDs, but significantly lower than that of the neat **9**-based OLEDs. We found, however, that the film of the mixture is quite homogeneous, without crystallization signs, which is probably the reason why the current shows a smoother variation with the applied voltage when compared with that of neat **7**-based OLEDs. The EL spectra for the three devices structures are very similar, as shown in Figure S40C).

It should be mentioned that OLEDs based on the dispersion of this **7+9** mixture in PVK do not show improved performance (maximum luminance of 14 cd m⁻², maximum electroluminescence efficiency of 0.010 cd A⁻¹).

Table S9. Electroluminescence data for OLEDs prepared by spin coating of either THF solutions of the neat complexes or THF solutions of the complexes mixed with PVK. The general OLEDs structure was ITO/PEDOT:PSS/active layer/Ca/Al. Devices containing an interlayer (IL) of polyTPD, between PEDOT:PSS and the active layer, were also fabricated and tested. Pixel areas were 8 mm², except for some identified cases, where a 4 mm² area was used.

	5	6	7	8	9
					
ϕ_{r} (THF solution)	0.32	0.40	0.32	0.34 ^b	0.36
ϕ_{PL} (ZEONEX film)	0.31	0.40	0.31	0.37	0.36
Neat complexes	Negligible	$L^{\text{max}}=10 \text{ cd m}^{-2}$ $\phi_{\text{EL}}^{\text{max}}=0.003 \text{ cd A}^{-1}$ $\text{EQE}^{\text{max}}=0.001 \%$ $\text{EL}^{\text{max}}=485 \text{ nm}^a$	$L^{\text{max}}=43 \text{ cd m}^{-2}$ $\phi_{\text{EL}}^{\text{max}}=0.013 \text{ cd A}^{-1}$ $\text{EQE}^{\text{max}}=0.004\%$ $\text{EL}^{\text{max}}=564 \text{ nm}^a$	$L^{\text{max}}=0.35 \text{ cd m}^{-2}$ $\phi_{\text{EL}}^{\text{max}}=3.8 \times 10^{-4} \text{ cd A}^{-1}$ $\text{EQE}^{\text{max}}=1.5 \times 10^{-4} \%$ $\text{EL}^{\text{max}}=490 \text{ nm}^{a,b}$	$L^{\text{max}}=958 \text{ cd m}^{-2}$ $\phi_{\text{EL}}^{\text{max}}=0.30 \text{ cd A}^{-1}$ $\text{EQE}^{\text{max}}=0.084\%$ $\text{EL}^{\text{max}}=531 \text{ nm}^{a,c}$
PVK + 4% complexes	$L^{\text{max}}=79 \text{ cd m}^{-2}$ $\phi_{\text{EL}}^{\text{max}}=0.087 \text{ cd A}^{-1}$ $\text{EQE}^{\text{max}}=0.032\%$ $\text{EL}^{\text{max}}=502 \text{ nm}$	$L^{\text{max}}=41 \text{ cd m}^{-2}$ $\phi_{\text{EL}}^{\text{max}}=0.0065 \text{ cd A}^{-1}$ $\text{EQE}^{\text{max}}=0.0029 \%$ $\text{EL}^{\text{max}}=483 \text{ nm}$	$L^{\text{max}}=31 \text{ cd m}^{-2}$ $\phi_{\text{EL}}^{\text{max}}=0.020 \text{ cd A}^{-1}$ $\text{EQE}^{\text{max}}=0.0065\%$ $\text{EL}^{\text{max}}=524 \text{ nm}$	-	$L^{\text{max}}=94 \text{ cd m}^{-2}$ $\phi_{\text{EL}}^{\text{max}}=0.0281 \text{ cd A}^{-1}$ $\text{EQE}^{\text{max}}=0.0092\%$ $\text{EL}^{\text{max}}=522 \text{ nm}$
polyTPD_IL/PVK + 4% complexes	$L^{\text{max}}=31 \text{ cd m}^{-2}$ $\phi_{\text{EL}}^{\text{max}}=0.025 \text{ cd A}^{-1}$ $\text{EQE}^{\text{max}}=0.0093\%$ $\text{EL}^{\text{max}}=498 \text{ nm}$	$L^{\text{max}}=170 \text{ cd m}^{-2}$ $\phi_{\text{EL}}^{\text{max}}=0.037 \text{ cd A}^{-1}$ $\text{EQE}^{\text{max}}=0.016\%$ $\text{EL}^{\text{max}}=485 \text{ nm}$	$L^{\text{max}}=40 \text{ cd m}^{-2}$ $\phi_{\text{EL}}^{\text{max}}=0.0074 \text{ cd A}^{-1}$ $\text{EQE}^{\text{max}}=0.0023\%$ $\text{EL}^{\text{max}}=524 \text{ nm}$	-	$L^{\text{max}}=124 \text{ cd m}^{-2}$ $\phi_{\text{EL}}^{\text{max}}=0.026 \text{ cd A}^{-1}$ $\text{EQE}^{\text{max}}=0.0085\%$ $\text{EL}^{\text{max}}=522 \text{ nm}$

^a Pixel area of 4 mm²; ^b Ref. 11c; ^c Ref. 11d

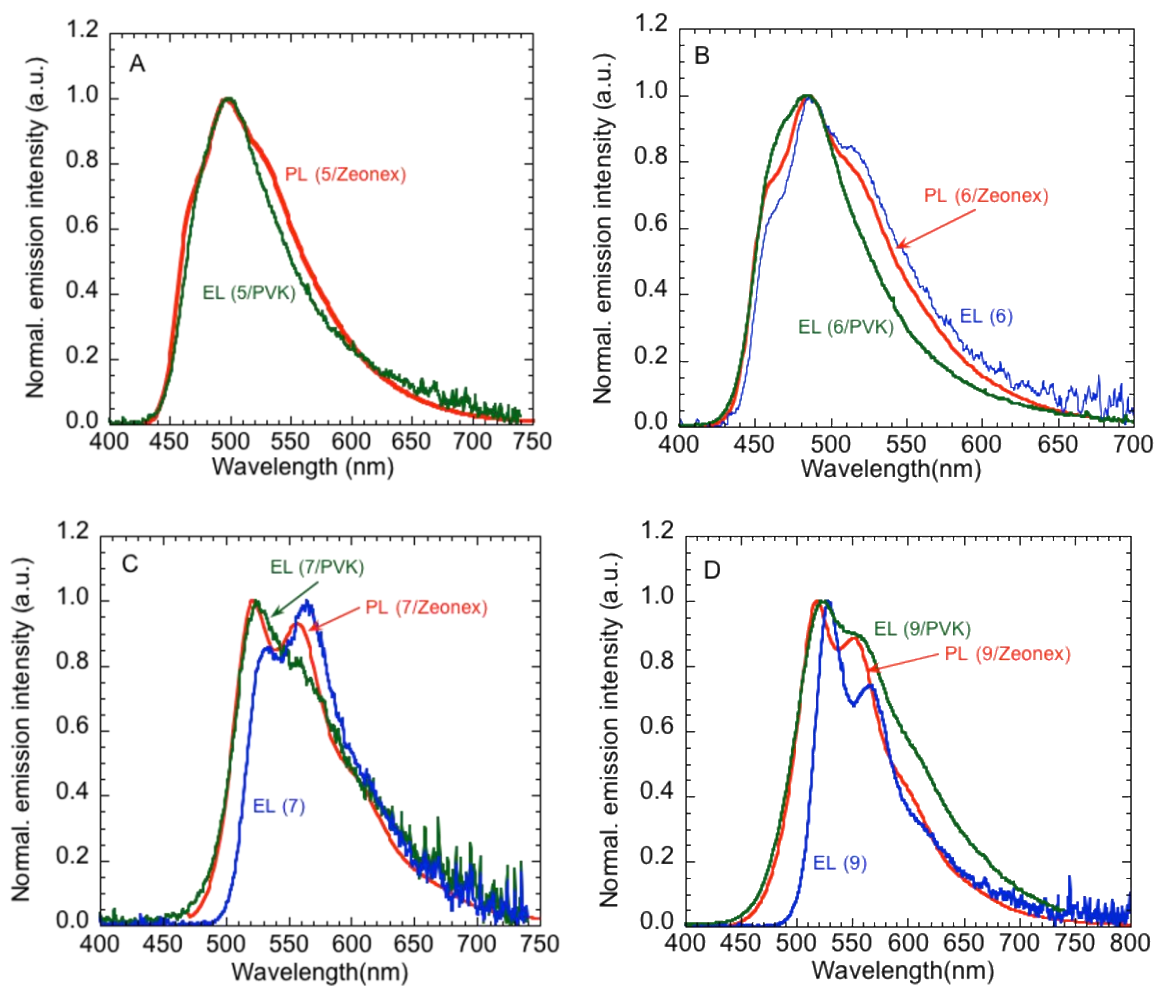


Fig. S39. Comparison between the EL spectra recorded from the OLEDs based on active layers made of both the complexes dispersed in PVK and the neat complexes and the PL spectra recorded for the complexes dispersed in ZEONEX.

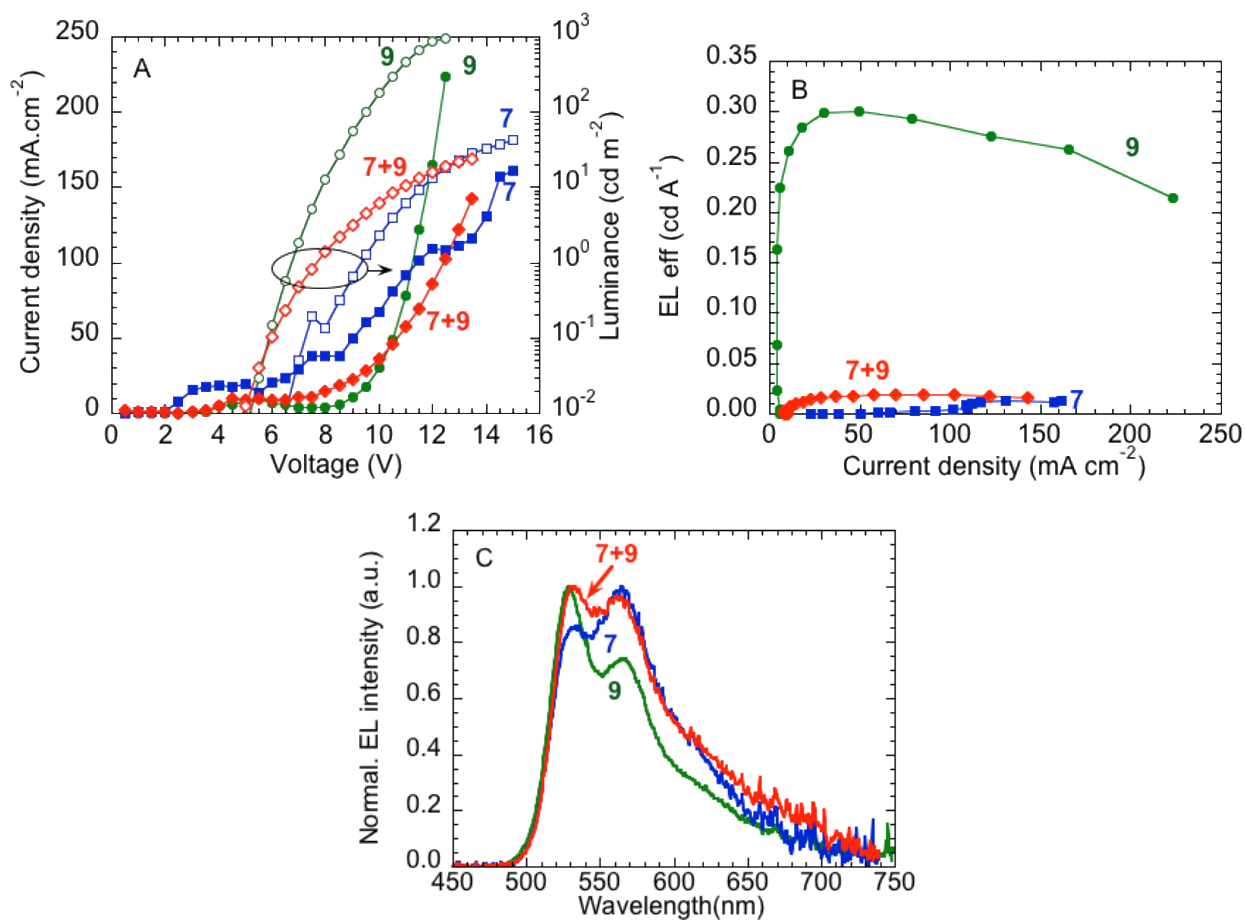


Fig. S40. Characteristics of the OLEDs based on neat complexes **7** and **9** with those of the OLED based on their mixture. A) Current density (closed symbols) and luminance as a function of the applied voltage; B) Electroluminescence efficiency as a function of the current density in the devices; and C) EL spectra.